Cross-correlation of Dark Energy Survey Year 3 lensing data with ACT and *Planck* thermal Sunyaev-Zel'dovich effect observations. I. Measurements, systematics tests, and feedback model constraints

M. Gatti,[1,*] S. Pandey,[1] E. Baxter,[2] J. C. Hill,[3,4] E. Moser,[5] M. Raveri,[1] X. Fang,[6] J. DeRose,[7] G. Giannini,[8] C. Doux,[1] H. Huang,[9] N. Battaglia,[5] A. Alarcon,[10] A. Amon,[11] M. Becker,[10] A. Campos,[12] C. Chang,[13,14] R. Chen,[15] A. Choi,[16] K. Eckert,[1] J. Elvin-Poole,[16,17] S. Everett,[18] A. Ferte,[19] I. Harrison,[20,21] N. Maccrann,[22] J. Mccullough,[11] J. Myles,[23,11,24] A. Navarro Alsina,[25] J. Prat,[13,14] R. P. Rollins,[21] C. Sanchez,[1] T. Shin,[1] M. Troxel,[15] I. Tutusaus,[26,27] B. Yin,[12] T. Abbott,[28] M. Aguena,[29] S. Allam,[30] F. Andrade-Oliveira,[31,29] J. Annis,[30] G. Bernstein,[1] E. Bertin,[32,33] B. Bolliet,[3] J. R. Bond,[34] D. Brooks,[35,11,24] D. L. Burke,[11,24] E. Calabrese,[36] A. Carnero Rosell,[37,29,38] M. Carrasco Kind,[39,40] J. Carretero,[8] R. Cawthon,[41] M. Costanzi,[42,43,44] M. Crocce,[26,27] L. N. da Costa,[29,45] M. E. da Silva Pereira,[46] J. De Vicente,[47] S. Desai,[48] H. T. Diehl,[30] J. P. Dietrich,[49] P. Doel,[35] J. Dunkley,[50,51] A. E. Evrard,[52,46] S. Ferraro,[53,54] I. Ferrero,[55] B. Flaugher,[30] P. Fosalba,[26,27] J. Frieman,[30,14] J. García-Bellido,[56] E. Gaztanaga,[26,27] D. W. Gerdes,[52,46] T. Giannantonio,[57,58] D. Gruen,[49] R. A. Gruendl,[39,40] J. Gschwend,[29,45] G. Gutierrez,[30] K. Herner,[30] A. D. Hincks,[59] S. R. Hinton,[60] D. L. Hollowood,[18] K. Honscheid,[16,17] J. P. Hughes,[61] D. Huterer,[46] B. Jain,[1] D. J. James,[62] E. Krause,[6] K. Kuehn,[63,64] N. Kuropatkin,[30] O. Lahav,[35] C. Lidman,[65,66] M. Lima,[67,29] M. Lokken,[59,34,68] M. S. Madhavacheril,[69] M. A. G. Maia,[29,45] J. L. Marshall,[70] J. J. Mcmahon,[71,72,73,74] P. Melchior,[50] K. Moodley,[75,76] J. J. Mohr,[49,77] R. Morgan,[41] F. Nati,[78] M. D. Niemack,[5,5,79] L. Page,[51] A. Palmese,[30,14] F. Paz-Chinchón,[39,57] A. Pieres,[29,45] A. A. Plazas Malagón,[50] M. Rodriguez-Monroy,[47] A. K. Romer,[80] E. Sanchez,[47] V. Scarpine,[30] E. Schaan,[53,54] L. F. Secco,[1,14] S. Serrano,[26,27] E. Sheldon,[81] B. D. Sherwin,[82,58] C. Sifón,[83] M. Smith,[84] M. Soares-Santos,[46] D. Spergel,[4,85] E. Suchyta,[86] G. Tarle,[46] D. Thomas,[87] C. To,[23,11,24] D. L. Tucker,[30] T. N. Varga,[77,88] J. Weller,[77,88] R. D. Wilkinson,[80] E. J. Wollack,[89] and Z. Xu[90,1]

(DES and ACT Collaboration)

[1]*Department of Physics and Astronomy, University of Pennsylvania, Philadelphia, Pennsylvania 19104, USA*
[2]*Institute for Astronomy, University of Hawai'i, 2680 Woodlawn Drive, Honolulu, Hawai'i 96822, USA*
[3]*Department of Physics, Columbia University, New York, New York 10027, USA*
[4]*Center for Computational Astrophysics, Flatiron Institute, New York, New York 10010, USA*
[5]*Department of Astronomy, Cornell University, Ithaca, New York 14853, USA*
[6]*Department of Astronomy/Steward Observatory, University of Arizona, 933 North Cherry Avenue, Tucson, Arizona 85721-0065, USA*
[7]*Lawrence Berkeley National Laboratory, 1 Cyclotron Road, Berkeley, California 94720, USA*
[8]*Institut de Física d'Altes Energies (IFAE), The Barcelona Institute of Science and Technology, Campus UAB, 08193 Bellaterra (Barcelona), Spain*
[9]*Department of Physics, University of Arizona, Tucson, Arizona 85721, USA*
[10]*Argonne National Laboratory, 9700 South Cass Avenue, Lemont, Illinois 60439, USA*
[11]*Kavli Institute for Particle Astrophysics and Cosmology, P. O. Box 2450, Stanford University, Stanford, California 94305, USA*
[12]*Department of Physics, Carnegie Mellon University, Pittsburgh, Pennsylvania 15312, USA*
[13]*Department of Astronomy and Astrophysics, University of Chicago, Chicago, Illinois 60637, USA*
[14]*Kavli Institute for Cosmological Physics, University of Chicago, Chicago, Illinois 60637, USA*
[15]*Department of Physics, Duke University, Durham, North Carolina 27708, USA*
[16]*Center for Cosmology and Astro-Particle Physics, The Ohio State University, Columbus, Ohio 43210, USA*
[17]*Department of Physics, The Ohio State University, Columbus, Ohio 43210, USA*
[18]*Santa Cruz Institute for Particle Physics, Santa Cruz, California 95064, USA*
[19]*Jet Propulsion Laboratory, California Institute of Technology, 4800 Oak Grove Drive, Pasadena, California 91109, USA*
[20]*Department of Physics, University of Oxford, Denys Wilkinson Building, Keble Road, Oxford OX1 3RH, United Kingdom*
[21]*Jodrell Bank Center for Astrophysics, School of Physics and Astronomy, University of Manchester, Oxford Road, Manchester M13 9PL, United Kingdom*
[22]*Department of Applied Mathematics and Theoretical Physics, University of Cambridge, Cambridge CB3 0WA, United Kingdom*

[23]*Department of Physics, Stanford University, 382 Via Pueblo Mall, Stanford, California 94305, USA*
[24]*SLAC National Accelerator Laboratory, Menlo Park, California 94025, USA*
[25]*Instituto de Física Gleb Wataghin, Universidade Estadual de Campinas, 13083-859 Campinas, São Paulo, Brazil*
[26]*Institut d'Estudis Espacials de Catalunya (IEEC), 08034 Barcelona, Spain*
[27]*Institute of Space Sciences (ICE, CSIC), Campus UAB, Carrer de Can Magrans, s/n, 08193 Barcelona, Spain*
[28]*Cerro Tololo Inter-American Observatory, NSF's National Optical-Infrared Astronomy Research Laboratory, Casilla 603, La Serena, Chile*
[29]*Laboratório Interinstitucional de e-Astronomia - LIneA, Rua Gal. José Cristino 77, Rio de Janeiro, RJ - 20921-400, Brazil*
[30]*Fermi National Accelerator Laboratory, P. O. Box 500, Batavia, Illinois 60510, USA*
[31]*Instituto de Física Teórica, Universidade Estadual Paulista, 01140-070 São Paulo, Brazil*
[32]*CNRS, UMR 7095, Institut d'Astrophysique de Paris, F-75014 Paris, France*
[33]*Sorbonne Universités, UPMC University Paris 06, UMR 7095, Institut d'Astrophysique de Paris, F-75014 Paris, France*
[34]*Canadian Institute for Theoretical Astrophysics, 60 St. George Street, University of Toronto, Toronto, Ontario M5S 3H8, Canada*
[35]*Department of Physics and Astronomy, University College London, Gower Street, London WC1E 6BT, United Kingdom*
[36]*School of Physics and Astronomy, Cardiff University, The Parade, Cardiff CF24 3AA, United Kingdom*
[37]*Instituto de Astrofisica de Canarias, E-38205 La Laguna, Tenerife, Spain*
[38]*Universidad de La Laguna, Departamento Astrofísica, E-38206 La Laguna, Tenerife, Spain*
[39]*Center for Astrophysical Surveys, National Center for Supercomputing Applications, 1205 West Clark Street, Urbana, Illinois 61801, USA*
[40]*Department of Astronomy, University of Illinois at Urbana-Champaign, 1002 West Green Street, Urbana, Illinois 61801, USA*
[41]*Physics Department, 2320 Chamberlin Hall, University of Wisconsin-Madison, 1150 University Avenue, Madison, Wisconsin 53706-1390, USA*
[42]*Astronomy Unit, Department of Physics, University of Trieste, via Tiepolo 11, I-34131 Trieste, Italy*
[43]*INAF-Osservatorio Astronomico di Trieste, via G. B. Tiepolo 11, I-34143 Trieste, Italy*
[44]*Institute for Fundamental Physics of the Universe, Via Beirut 2, 34014 Trieste, Italy*
[45]*Observatório Nacional, Rua Gal. José Cristino 77, Rio de Janeiro, RJ - 20921-400, Brazil*
[46]*Department of Physics, University of Michigan, Ann Arbor, Michigan 48109, USA*
[47]*Centro de Investigaciones Energéticas, Medioambientales y Tecnológicas (CIEMAT), 28040 Madrid, Spain*
[48]*Department of Physics, IIT Hyderabad, Kandi, Telangana 502285, India*
[49]*Faculty of Physics, Ludwig-Maximilians-Universität, Scheinerstrasse 1, 81679 Munich, Germany*
[50]*Department of Astrophysical Sciences, Princeton University, Peyton Hall, Princeton, New Jersey 08544, USA*
[51]*Department of Physics, Jadwin Hall, Princeton University, Princeton, New Jersey 08544-0708, USA*
[52]*Department of Astronomy, University of Michigan, Ann Arbor, Michigan 48109, USA*
[53]*Lawrence Berkeley National Laboratory, One Cyclotron Road, Berkeley, California 94720, USA*
[54]*Berkeley Center for Cosmological Physics, University of California, Berkeley, California 94720, USA*
[55]*Institute of Theoretical Astrophysics, University of Oslo, P.O. Box 1029 Blindern, NO-0315 Oslo, Norway*
[56]*Instituto de Fisica Teorica UAM/CSIC, Universidad Autonoma de Madrid, 28049 Madrid, Spain*
[57]*Institute of Astronomy, University of Cambridge, Madingley Road, Cambridge CB3 0HA, United Kingdom*
[58]*Kavli Institute for Cosmology, University of Cambridge, Madingley Road, Cambridge CB3 0HA, United Kingdom*
[59]*David A. Dunlap Department of Astronomy and Astrophysics, University of Toronto, 50 St. George Street, Toronto, Ontario M5S 3H4, Canada*
[60]*School of Mathematics and Physics, University of Queensland, Brisbane, Queensland 4072, Australia*
[61]*Department of Physics and Astronomy, Rutgers, the State University of New Jersey, 136 Frelinghuysen Road, Piscataway, New Jersey 08854-8019, USA*
[62]*Center for Astrophysics | Harvard and Smithsonian, 60 Garden Street, Cambridge, Massachusetts 02138, USA*
[63]*Australian Astronomical Optics, Macquarie University, North Ryde, New South Wales 2113, Australia*
[64]*Lowell Observatory, 1400 Mars Hill Road, Flagstaff, Arizona 86001, USA*

[65]*Centre for Gravitational Astrophysics, College of Science, The Australian National University, Australian Capital Territory 2601, Australia*
[66]*The Research School of Astronomy and Astrophysics, Australian National University, Australian Capital Territory 2601, Australia*
[67]*Departamento de Física Matemática, Instituto de Física, Universidade de São Paulo, CP 66318, São Paulo, SP 05314-970, Brazil*
[68]*Dunlap Institute of Astronomy and Astrophysics, 50 St. George Street, Toronto, Ontario M5S 3H4, Canada*
[69]*Perimeter Institute for Theoretical Physics, 31 Caroline Street North, Waterloo, Ontario N2L 2Y5, Canada*
[70]*Department of Physics and Astronomy, George P. and Cynthia Woods Mitchell Institute for Fundamental Physics and Astronomy, Texas A&M University, College Station, Texas 77843, USA*
[71]*Department of Astronomy and Astrophysics, University of Chicago, 5640 South Ellis Avenue, Chicago, Illinois 60637, USA*
[72]*Kavli Institute for Cosmological Physics, University of Chicago, 5640 South Ellis Avenue, Chicago, Illinois 60637, USA*
[73]*Department of Physics, University of Chicago, Chicago, Illinois 60637, USA*
[74]*Enrico Fermi Institute, University of Chicago, Chicago, Illinois 60637, USA*
[75]*Astrophysics Research Centre, University of KwaZulu-Natal, Westville Campus, Durban 4041, South Africa*
[76]*School of Mathematics, Statistics and Computer Science, University of KwaZulu-Natal, Westville Campus, Durban 4041, South Africa*
[77]*Max Planck Institute for Extraterrestrial Physics, Giessenbachstrasse, 85748 Garching, Germany*
[78]*Department of Physics, University of Milano-Bicocca, Piazza della Scienza 3, 20126 Milano (MI), Italy*
[79]*Kavli Institute at Cornell for Nanoscale Science, Cornell University, Ithaca, New York 14853, USA*
[80]*Department of Physics and Astronomy, Pevensey Building, University of Sussex, Brighton BN1 9QH, United Kingdom*
[81]*Brookhaven National Laboratory, Building 510, Upton, New York 11973, USA*
[82]*Department of Applied Mathematics and Theoretical Physics, University of Cambridge, Cambridge CB3 0WA, United Kingdom*
[83]*Instituto de Física, Pontificia Universidad Católica de Valparaíso, Casilla 4059, Valparaíso, Chile*
[84]*School of Physics and Astronomy, University of Southampton, Southampton SO17 1BJ, United Kingdom*
[85]*Department of Astrophysical Sciences, Princeton University, Princeton, New Jersey 08544, USA*
[86]*Computer Science and Mathematics Division, Oak Ridge National Laboratory, Oak Ridge, Tennessee 37831, USA*
[87]*Institute of Cosmology and Gravitation, University of Portsmouth, Portsmouth PO1 3FX, United Kingdom*
[88]*Universitäts-Sternwarte, Fakultät für Physik, Ludwig-Maximilians Universität München, Scheinerstrasse 1, 81679 München, Germany*
[89]*NASA Goddard Space Flight Center, 8800 Greenbelt Road, Greenbelt, Maryland 20771, USA*
[90]*MIT Kavli Institute, Massachusetts Institute of Technology, 77 Massachusetts Avenue, Cambridge, Massachusetts 02139, USA*

(Received 8 September 2021; accepted 24 April 2022; published 21 June 2022)

We present a tomographic measurement of the cross-correlation between thermal Sunyaev-Zel'dovich (TSZ) maps from *Planck* and the Atacama Cosmology Telescope and weak galaxy lensing shears measured during the first three years of observations of the Dark Energy Survey. This correlation is sensitive to the thermal energy in baryons over a wide redshift range and is therefore a powerful probe of astrophysical feedback. We detect the correlation at a statistical significance of 21σ, the highest significance to date. We examine the TSZ maps for potential contaminants, including cosmic infrared background and radio sources, finding that cosmic infrared background has a substantial impact on our measurements and must be taken into account in our analysis. We use the cross-correlation measurements to test different feedback models. In particular, we model the TSZ using several different pressure profile models calibrated against hydrodynamical simulations. Our analysis marginalizes over redshift uncertainties, shear calibration biases, and intrinsic alignment effects. We also marginalize over Ω_m and σ_8 using *Planck* or DES priors. We find that the data prefer the model with a low amplitude of the pressure profile at small scales, compatible with a

*marcogatti29@gmail.com

scenario with strong active galactic nuclei feedback and ejection of gas from the inner part of the halos. When using a more flexible model for the shear profile, constraints are weaker, and the data cannot discriminate between different baryonic prescriptions.

DOI: 10.1103/PhysRevD.105.123525

I. INTRODUCTION

The cosmic microwave background (CMB) provides a means to study early Universe physics as well as a powerful tool with which to probe the properties of the late Universe. As photons travel through cosmic time, they are affected by the large-scale structure of the Universe at low redshift, which leaves an imprint on the CMB. Among these so-called "secondary anisotropies," generated after photons leave the surface of last scattering, the imprints left by the thermal Sunyaev-Zel'dovich (TSZ) effect [1,2] are some of the most important. The effect is caused by inverse Compton scattering of CMB photons with ionized gas. The TSZ effect is an effective probe of large-scale structure, as the signal is sensitive to the halo mass function, which in turn strongly depends on the amplitude of the matter fluctuations, i.e., σ_8, and on the matter density Ω_m [3]. It is also an effective probe of the properties of the hot gas within and outside dark-matter halos, as the measured signal depends on the hot gas pressure profile.

A better understanding of the properties of baryons within dark-matter halos is needed to fully exploit the cosmological information from the small-scale regime in current and future cosmological analyses [Dark Energy Survey (DES), Flaugher *et al.* [4]; Kilo-Degree Survey, Kuijken *et al.* [5]; Hyper Suprime-Cam (HSC), Aihara *et al.* [6]; Rubin Observatory Legacy Survey of Space and Time, Legacy Survey of Space and Time (LSST) Science Collaboration *et al.* [7]; Euclid, Laureijs *et al.* [8]]. Astrophysical feedback significantly impacts the baryons, leading to changes in the matter power spectrum at small scales [9–11]. Ignoring such effects can lead to significant biases in cosmological analyses [12–14].

Various strategies have been adopted to mitigate the impact of baryonic feedback on cosmological constraints. The most straightforward way is to exclude the scales that could be significantly affected by baryonic effects (e.g., Troxel *et al.* [15]). Other methods include adding extra complexity to the modeling to account for the effect of baryons [16–20], empirically modeling baryonic effects using fitting formulas calibrated against hydrodynamical simulations [21], or using principal component analysis and hydrodynamical simulations to identify the modes of the data vector most sensitive to baryonic effects, and to marginalize over them [12,13,22]. As many of these mitigation strategies rely more or less directly on hydrodynamical simulations, the specific details of the implementation of baryonic physics in such simulations also have an impact on these methods.

Analysis of the TSZ effect provides a potential means for setting priors on different baryonic feedback prescriptions or to promote or rule out some of the hydrodynamical simulations. Particularly appealing are studies that involve the cross-correlation of the TSZ effect with other probes sensitive to large-scale structure. Such cross-correlations have different sensitivity to nuisance parameters that makes these measurements less prone to systematics. Moreover, cross-correlations with different probes are key to study the evolution of baryonic effects with redshift or their dependence on the environment and the halo mass. In this work we focus on cross-correlations between the TSZ effect and weak gravitational lensing, a measurement that has gained attention over the last few years. Van Waerbeke *et al.* [23] obtained the first detection of the cross-correlation signal between the shear field and a Compton-y measurement, using a Canada France Hawaii Telescope (CFHT) lensing convergence map and a Compton-y map built using *Planck* data. In the following year, Hill and Spergel [24] measured the TSZ $\times$ CMB lensing signal for the first time, which is in spirit a similar measurement, although it probes a higher redshift range compared to [23]. Subsequently, other measurements have been performed by Hojjati *et al.* [25], who detected a cross-correlation signal using *Planck* data and a shape catalog from the RCSLenS survey, and by Osato *et al.* [26] using *Planck* and HSC data. For this work, we use the fiducial shape catalog for DES year three (DES Y3) data [27], and Compton-y maps from both *Planck* [28] and the Atacama Cosmology Telescope (ACT) [29].[1] The large area coverage by the DES Y3 weak lensing sample (4183 deg^2) allows us to considerably improve the signal-to-noise ratio of the measurement compared to previous studies. Moreover, the addition of the ACT map—which covers a smaller area compared to *Planck* but has a much higher spatial resolution—allows us to extend the measurement down to $\sim$2.5 arc min scales.

In this work and in a companion paper (Pandey *et al.* [30], hereafter paper II) we present the correlation measurements and perform several different analyses. We focus here on two aspects in particular:

(i) We discuss various systematic tests, with a focus on the effect of potential contaminants, i.e., the cosmic infrared background (CIB), and radio sources, and
(ii) we compare the measurements to theoretical predictions using the halo model framework and pressure

[1]The ACT Compton-y map is created using both low (spatial) resolution data from *Planck* and high resolution data from ACT, but for the sake of simplicity we refer to it as the ACT map. More details are given in Sec. II.

profiles as estimated from a number of hydrodynamical simulations, with the goal of discriminating between different baryonic feedback models.

The analysis performed in this paper treats the pressure profile predictions of hydrodynamical simulations as fixed and fits the data marginalizing over several nuisance parameters, modeling astrophysical and measurement systematics, including photometric redshift uncertainties, intrinsic alignment, and shear calibration biases. We also marginalize over cosmological parameters assuming *Planck* or DES priors. On the other hand, in paper II, we use an alternate approach:

(i) We fit the measurements by varying the parameters of a flexible model for the halo pressure profiles, exploring how the halo pressure profiles evolve as a function of halo mass and redshift, and
(ii) we discuss implications of our measurements on the constraints of the so-called halo mass bias parameter.

The paper is organized as follows. In Sec. II we describe the data used in this work. Section III describes the theoretical modeling of the measurement, introducing the feedback models considered in this work and the modeling choices of the analysis. Section IV B presents our *Planck* × DES and ACT × DES measurements, and systematic tests are discussed in Sec. IV C. We test different feedback models in Sec. IV D; we summarize our findings in Sec. V. We provide further validation of our modeling on N-body simulations in Appendix A; Appendix B shows our validation of the analytical covariance matrix; Appendix C illustrates the effect of CIB contamination on simulated Compton-y maps; last, Appendix D shows our results when DES priors for the cosmological parameters are assumed.

II. DATA PRODUCTS

A. *Planck* Compton map

We use the publicly available 2015 *Planck* high frequency instrument and low frequency instrument maps [31,32] to estimate the Compton-y map using the Needlet Internal Linear Combination (NILC) algorithm [33,34]. We build our own version of the *Planck* Compton-y map, also using different prescriptions to deproject (i.e., remove) the contamination by the CIB.

In particular, we use all the channels from 30 to 545 GHz. We do not include the frequency map at 857 GHz because (1) the calibration of this map is more uncertain than the other frequency maps; (2) the dust is much brighter in this map than in any of the other maps and there are large dust-related residuals found in NILC maps if the 857 GHz map is used [28]. We also estimate the Compton-y map excluding the 545 GHz channel to test the sensitivity of our results to the CIB, which is brightest at high frequencies. The details of the implementation of this algorithm are presented in Appendix A of Pandey *et al.* [35] and more details on the CIB contribution are given in Sec. IV C. We found that the signal obtained using our own version of the Compton-y map with no CIB deprojection was compatible with the signal obtained using the public *Planck* Compton-y map [28]. The maps come in HealPix format with a resolution of NSIDE = 2048. The *Planck*-y map resolution has an effective full width at half maximum (FWHM) of 10 arc min. When producing the Compton-y maps, we applied the standard *Planck* foreground mask, which limits the diffuse Galactic emission removing the most-contaminated ∼40% of the sky, mostly around the Galactic plane. We further applied the fiducial DES Y3 mask [36], which removes areas affected by astrophysical foregrounds (e.g., bright stars and large nearby galaxies) and "bad" regions with recognized data processing issues within the DES Y3 footprint. In the fiducial maps we did not mask radio sources; however, for the purpose of testing, we produced an alternate version of the maps by removing the pixels affected by radio sources detected by ACT (which detects sources to a fainter limit compared to *Planck*). Last, we removed the regions that have overlap with ACT data, since that part of the sky is covered by the ACT + *Planck* Compton-y map (described in the next section) and the latter is preferred as it comes at a higher spatial resolution. In order to avoid correlations between the two Compton-y maps during the analysis, we further cut out a buffer region of a few degrees of width between the two maps, as shown in Fig. 1. This reduces the covariance between the measurements obtained using the two maps. The final area covered by *Planck* data is 3423 deg^2.

B. ACT Compton map

We use Compton-y maps from the Atacama Cosmology Telescope, as presented in [29] as part of data release 4 (DR4). The maps are obtained by combining *Planck* maps from 30 to 545 GHz and ACT maps at 98 and 150 GHz, using an anisotropic internal linear combination (ILC) component separation approach in the 2D Fourier domain (slightly different from the one used to create *Planck* maps). The original ACT maps are converted to HealPix format using the PIXELL package[2]; the maps have a resolution of NSIDE = 8192, with a FWHM of 1.6 arc min. We only use data from the D56 region, which overlaps with DES data, for a total area of 394 deg^2, after applying the ACT and DES masks. In contrast to the *Planck* maps case, for ACT compact sources (like radio sources) are subtracted by default, and the subtraction is followed by an inpainting procedure that estimates the correct value of the pixels affected by the compact sources. The inpainting algorithm fills holes around compact sources by finding the maximum-likelihood solution for pixels within the hole constrained by the pixels in a context region around the hole [29]. For the purpose of testing, we also make use of versions of the ACT map with the CIB contribution deprojected (see Sec. IV C). Contrary to the *Planck* map

[2]https://github.com/simonsobs/pixell.

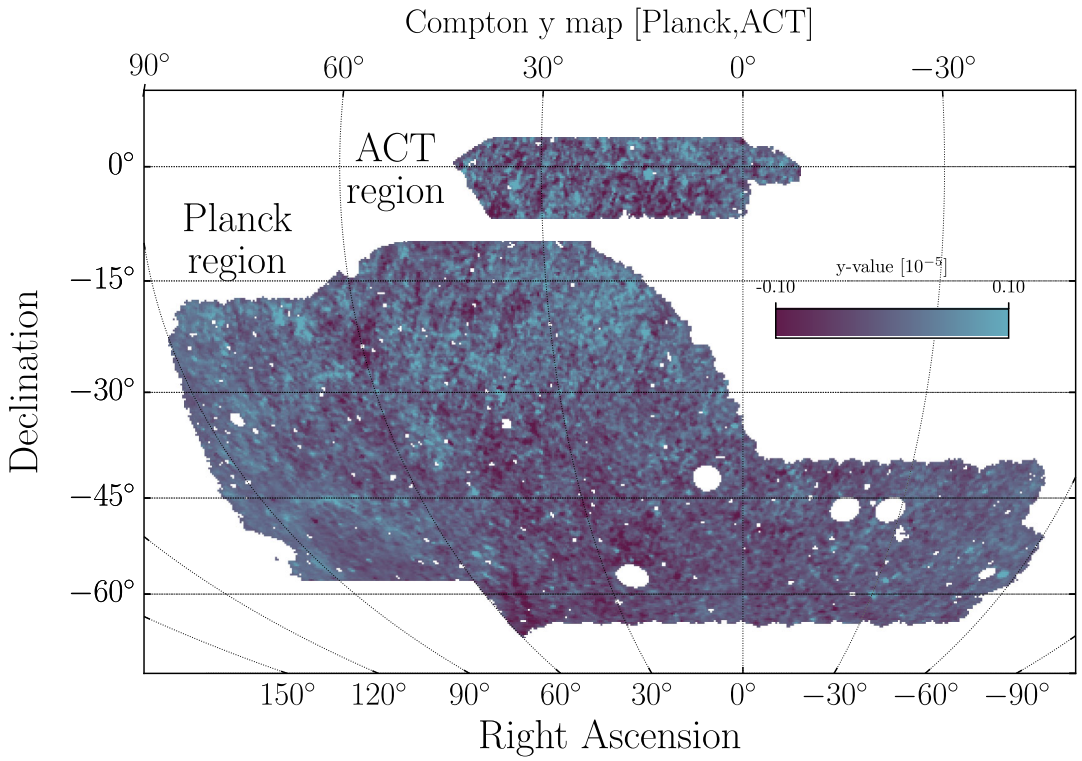

FIG. 1. *Planck* and ACT Compton-y maps after isolating the part of the maps that overlap with the DES Y3 footprint. A small "buffer" region between the two maps has been removed to reduce correlation between measurements in the two patches.

we do not create a version of the ACT Compton-y map excluding the 545 GHz frequency channel, as the fiducial ACT maps already assign a very small weight to this frequency channel.

C. DES Y3 data

We use the fiducial DES Y3 shape catalog, presented in [27]. The DES Y3 shape catalog is created using the Metacalibration pipeline, which is able to self-calibrate the measured shapes against shear and selection biases by measuring the mean shear and selection response matrix of the sample. The current DES Y3 implementation of Metacalibration [37,38] is able to correct for shear biases up to a multiplicative factor of 2%–3%, which is fully characterized using image simulations [39]. The final sample comprises 100×10^6 objects, for an effective number density of $n_{\rm eff} = 5.59$ gal/arc min^2, spanning an effective area of 4139 deg^2. Galaxies are further divided into four tomographic bins and redshift estimates for each of the tomographic bins are provided by the self-organizing map photo-z (SOMPZ) method [40]. The method uses additional information from deep fields [5] and spectroscopic samples to break degeneracies in the photo-z estimates of the wide field; this is achieved by creating self-organizing maps (SOMs) of the spectroscopic, deep, and wide field galaxies and mapping the three together. The redshift bin edges of the tomographic bins used for the tomographic bin assignments are $z = [0.0, 0.358, 0.631, 0.872, 2.0]$; wide field galaxies are assigned to different tomographic bins depending on the mean redshift of the cell of the deep SOM they are associated with. This assignment procedure, however, does not guarantee that the redshift distributions are sharply bounded (Fig. 2) Throughout this paper, we use the fiducial DES Y3 priors for the shear calibration biases and redshift uncertainties (see Sec. III D).

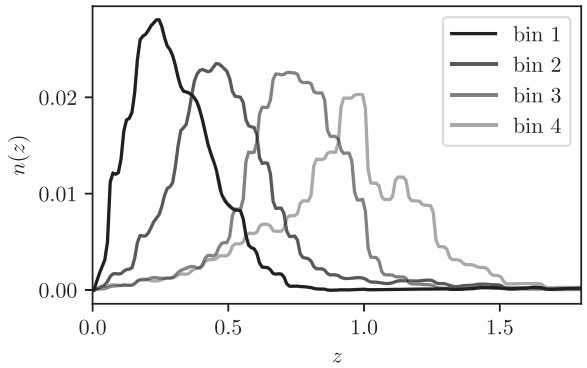

FIG. 2. Redshift distributions for the four DES Y3 tomographic bins [40].

III. THEORY

There exist different TSZ weak lensing cross-correlation estimators in the literature, both in configuration and

harmonic space (for a discussion on different estimators see, e.g., [25]). In this work we focus on a configuration space estimator, the $\xi^{\gamma_t y}$ correlation function, which has the advantage of not having complications induced by the presence of a mask, which usually affect harmonic space estimators [25]. Given a catalog of galaxy shapes and a Compton-y map, such an estimator is constructed by measuring the tangential shear around every point of the y map, weighted by the value of the y map, and by averaging all the measurements. This is repeated for different angular separations θ between the y map points and the galaxy shapes used to compute the tangential shear. This estimator has the advantage of being particularly robust to additive systematics in the shear data. The measured $\xi^{\gamma_t y}$ correlation signal can be theoretically modeled relying on the halo model framework [41]. Note that the validity of the halo model to describe shear-Compton-y cross-correlation measurements has been demonstrated by [42], using hydrodynamical simulations [43].

We begin by modeling correlations between the convergence field and Compton-y maps in harmonic space and then transform this model to obtain a prediction for the $\xi^{\gamma_t y}$ correlation signal in configuration space. In harmonic space, the correlation can be described as an effective sum of a one-halo term and a two-halo term, with the one-halo term given by an integral over redshift (z) and halo mass (M),

$$C_\ell^{\kappa,y;1h} = \int_{z_{\rm min}}^{z_{\rm max}} dz \frac{dV}{dz d\Omega} \int_{M_{\rm min}}^{M_{\rm max}} dM \frac{dn}{dM} \bar{\kappa}_\ell(M,z) \bar{y}_\ell(M,z), \tag{1}$$

where dV is the cosmological volume element, dn/dM is the halo mass function from [44], and $\bar{y}_\ell$ and $\bar{\kappa}_\ell$ are the harmonic space profiles of the Compton-y map and the lensing convergence, respectively. The two-halo term is given by

$$C_\ell^{\kappa,y;2h} = \int_{z_{\rm min}}^{z_{\rm max}} dz \frac{dV}{dz d\Omega} b_\ell^\kappa(z) b_\ell^y(z) P_{\rm lin}(k,z), \tag{2}$$

where $k = (\ell + 1/2)/\chi$, χ is the comoving distance to redshift z, $P_{\rm lin}(k,z)$ is the linear power spectrum, and b_ℓ^κ and b_ℓ^y are the effective linear bias parameters describing the clustering of the two tracers.

The total power spectrum is obtained by summing the one- and two-halo components,

$$C_\ell^{\kappa,y} = C_\ell^{\kappa,y;1h} + C_\ell^{\kappa,y;2h}. \tag{3}$$

The y-γ_t cross-correlation can then be written as (similar to [25] but without the flat-sky approximation)

$$\xi^{\gamma_t y}(\theta) = \int \frac{d\ell \ell}{2\pi} J_2(\ell\theta) C_\ell^{\kappa,y}, \tag{4}$$

where J_2 is the second order Bessel function of the first kind.

A. The halo pressure profile

The profile in harmonic space of the Compton-y map can be related to the pressure profile $P_e(x|M_{200c},z)$ via (see, e.g., [3,45,46])

$$\bar{y}_\ell(M_{200c},z) = b^j(\ell) \frac{4\pi r_{200c}}{l_{200c}^2} \frac{\sigma_T}{m_e c^2} \times \int_{x_{\rm min}}^{x_{\rm max}} dx\, x^2 P_e(x|M_{200c},z) \frac{\sin(\ell x/l_{200c})}{\ell x/l_{200c}}. \tag{5}$$

In the above equation we have defined $x = a(z)R/R_{200c}$, where $a(z)$ is the scale factor, R is the radius, and R_{200c} is the radius enclosing the spherical region in which the average density is 200 times the critical density at the respective redshift; moreover, we defined $l_{200c} = D_A/R_{200c}$, where D_A is the angular diameter distance to redshift z. We choose $x_{\rm min} = 10^{-3}$ and $x_{\rm max} = 4$, which ensures that the above integral captures the contribution to the pressure from the extended profile of hot gas. Last, the term $b^j(\ell) = \exp[-\ell(\ell+1)\sigma_j^2/2]$ captures the beam profile. Here $\sigma_j = \theta_j^{\rm FWHM}/\sqrt{8\ln 2}$ and we have $\theta_1^{\rm FWHM} = 10$ arc min and $\theta_2^{\rm FWHM} = 1.6$ for *Planck* and ACT, respectively. We note that since we are dealing with pixelized Compton-y maps, we should also take into account the pixel window function; in practice, since the size of the pixel is always smaller than $0.5\theta^{\rm FWHM}$, it can be safely neglected.

The effective TSZ bias b_ℓ^y is given by

$$b_\ell^y(z) = \int_{M_{\rm min}}^{M_{\rm max}} dM \frac{dn}{dM} \bar{y}_\ell(M,z) b_{\rm lin}(M,z), \tag{6}$$

where $b_{\rm lin}$ is the linear bias of halos with mass M at redshift z (in the halo model, the halos are biased tracers of the underlying linear matter field). We use the Tinker *et al.* [47] fitting function for halo bias as a function of mass and redshift.

In this work, we consider the following pressure profile models, calibrated against hydrodynamical simulations implementing different baryonic feedback prescriptions:

(i) The Battaglia *et al.* [43] (B12) pressure profile, calibrated against a suite of hydrodynamical TreePM-smoothed particle hydrodynamics simulations that include radiative cooling, star formation, supernova feedback, and active galactic nuclei (AGN) feedback;

(ii) the Le Brun *et al.* [48] REF model, calibrated against a version of the cosmo-OverWhelmingly Large Simulations (OWLs) simulations [49] that includes prescriptions for radiative cooling, stellar evolution,

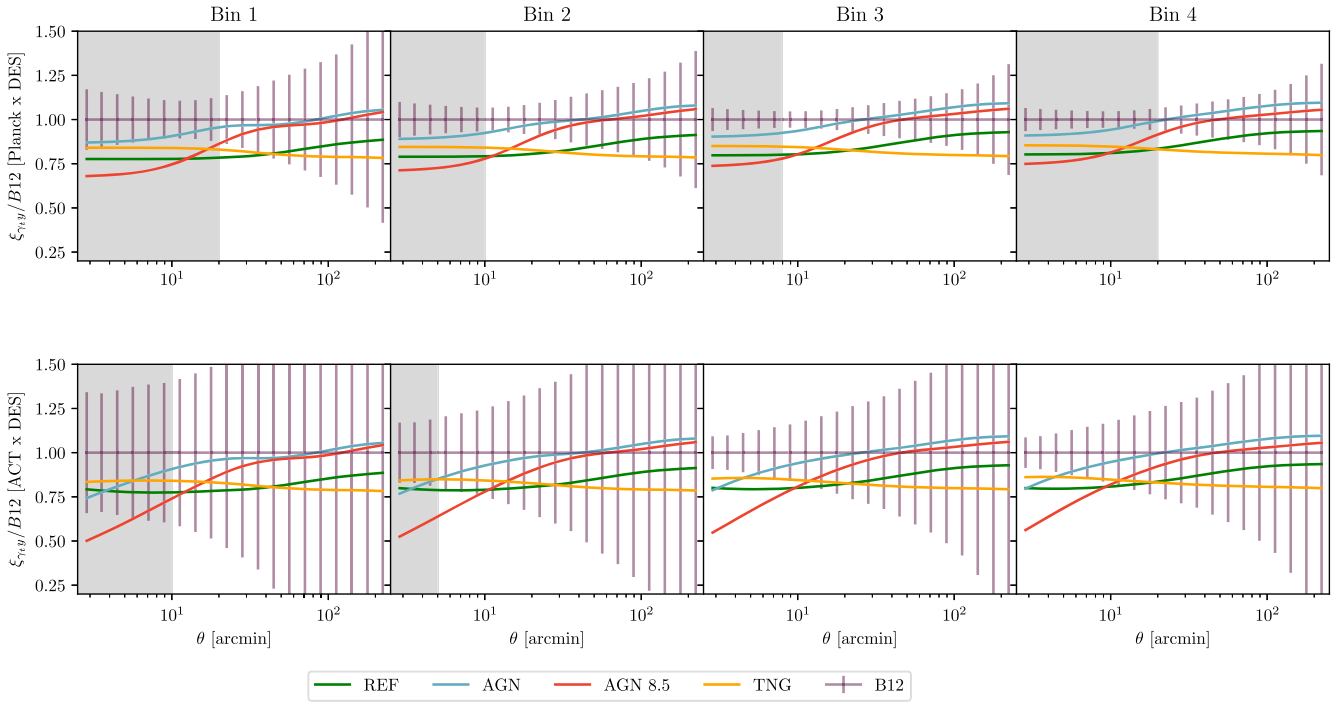

FIG. 3. Differences in the expected $\xi^{\gamma_t y}$ correlation signals assuming different pressure profile models, as introduced in Sec. III A. We take the predicted signal obtained with the B12 model as a reference. We show the predicted signals for the four tomographic bins of the DES shape catalog and for the two different Compton-y maps (ACT and *Planck*). For this figure, the shear part of the signal has been modeled assuming a Navarro-Frenk-White profile for the DM profile. Error bars for the B12 model show the expected measurement uncertainties; ACT measurement uncertainties are larger than *Planck* because of the smaller sky coverage. Gray shaded regions indicate the scales that are not used in this analysis (Table II). The error bars are strongly correlated between bins (adjacent bins are 60%–80% correlated, see Fig. 12 of paper II).

mass loss, chemical enrichment, and kinetic stellar feedback;

(iii) the Le Brun *et al.* [48] AGN model, calibrated against a version of the cosmo-OWLs simulations that also includes a prescription for AGN feedback. In particular, we include the two variants, the AGN and AGN 8.5 models, with the latter being characterized by a stronger AGN feedback prescription;

(iv) the pressure profile as measured in the IllustrisTNG simulation (TNG hereafter; Springel *et al.* [50]). The pressure profile is modeled as a generalized Navarro-Frenk-White (NFW) profile [51] similar to the B12 model, but fitting the model parameters (as well as their halo mass and redshift evolution) to the pressure profiles measured in the IllustrisTNG simulation.[3]

These are a wide range of hydrodynamical simulations with (more or less) different AGN prescriptions (see, e.g., EAGLE simulation [53], Horizon simulation [9], BAHAMAS simulation [54], etc.); measuring and comparing to all the pressure profiles from these simulations goes beyond the scope of this work. Moreover, we believe the profiles considered here already span a sufficiently wide range of different feedback models.

It is important to note that we are not interested here in freeing the parameters of the pressure profile models developed by Battaglia *et al.* [43] and Le Brun *et al.* [48], but rather we want to use their best-fit values to test whether the feedback mechanisms implemented in the simulations provide a good description of our measurement (within uncertainties). A different approach, where the pressure profile parameters are varied, is adopted in paper II.

We show how different pressure profile models translate to differences in the expected $\xi^{\gamma_t y}$ correlation signals in Fig. 3 (see also Fig. 4 for the expected amplitude of the signal). Different predictions are obtained via Eq. (4), assuming fiducial values for all the ingredients of the modeling except for the pressure profiles. For this comparison, the shear part of the signal has been modeled assuming a NFW profile for the dark matter (DM) profile (we note, however, that when analyzing our data we would also allow the DM profile to vary under the effects of baryons, as explained in the next section). We show the $\xi^{\gamma_t y}$

[3]In particular, we followed [52] and measured the pressure profile parameters dividing the halos of the simulations in two halo mass bins ($M \sim 10^{13.5}$–$10^{14.25}$ $M_\odot$, $M \sim 10^{14.25}$–$10^{15.0}$ $M_\odot$) and at three different redshift ($z = 0$, 0.31, 0.6) and interpolated the mass/redshift dependence. We could not use more bins due to the paucity of halos in this mass and redshift range.

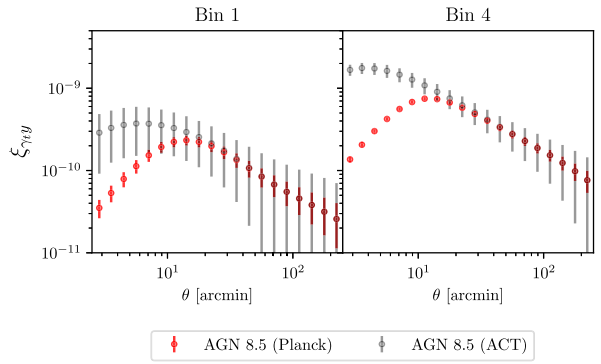

FIG. 4. Expected $\xi^{\gamma_t y}$ correlation signals for the ACT × DES (gray) and *Planck* × DES (red) measurements, assuming AGN 8.5 feedback model, as introduced in Sec. III A. We just show the first and the fourth bin; error bars represent measurement uncertainties. The dampening of the signal predicted for the *Planck* map at small scales is due to the large *Planck* beam.

correlation signals for the *Planck* and ACT Compton-y maps with the four tomographic bins of the DES shape catalog. The modeling of the *Planck* × DES and ACT × DES measurements differ only in the amplitude of the FWHM of the beam. We take the B12 model as a reference. The REF model is characterized by a 10%–20% lower amplitude at all angular scales and for all the different redshifts. In this model, a large fraction of halo baryons is able to cool and form stars, reducing the gas fraction and the TSZ amplitude. On the other hand, the two AGN models show a similar amplitude to the B12 model at large scales, but the most extreme AGN model (8.5) shows a significant lower amplitude (down to ∼40% in the ACT × DES measurement) at small scales, related to the gas ejection from the halo due to AGN feedback. Last, the TNG AGN model, which is based on a different suite of simulations and different AGN feedback mechanism compared to all the other models, is characterized by a 20% lower amplitude at all scales. The TNG AGN feedback is neither able to heat up the gas as much as the B12 model, resulting in a lower amplitude at all scales, nor to eject the gas from the halo as efficiently as the most extreme AGN 8.5 scenario (which would cause a lower amplitude at small scales).

B. Shear signal

The lensing part of our signal is described by the profile of the lensing convergence in harmonic space,

$$\bar{\kappa}_\ell(M_{\rm vir}, z) = \frac{W^\kappa(z)}{\chi^2} u_{\rm m}(k, M_{\rm vir}), \tag{7}$$

where $k = (\ell + 1/2)/\chi$ and $u_m(k, M)$ is the Fourier transformation of the dark-matter density profile. The quantity $W^\kappa(z(\chi))$ is the lensing kernel, given by

$$W^\kappa(z(\chi)) = \frac{3H_0^2\Omega_m}{2c^2}\frac{\chi}{a(\chi)}\int_\chi^\infty d\chi' n_\kappa(z(\chi'))\frac{dz}{d\chi'}\frac{\chi'-\chi}{\chi'}, \tag{8}$$

with n_κ the normalized redshift distribution of the source galaxies. The redshift distribution of the source galaxies peaks at significantly higher redshift compared to the sensitivity of our signal (see Fig. 2 of paper II); this implies that the dilution of the signal due to sources physically associated with foreground clusters [55,56] is negligible. The effective lensing bias is

$$b_\ell^\kappa(z) = \int_{M_{\rm min}}^{M_{\rm max}} dM \frac{dn}{dM}\bar{\kappa}_\ell(M, z) b_{\rm lin}(M, z), \tag{9}$$

where $b_{\rm lin}$ is the linear bias of halos with mass M at redshift z which we model using the Tinker *et al.* [47] fitting function. In case of no feedback, the dark-matter profile can be modeled by a simple NFW profile [51], but in practice baryonic feedback can affect the overall matter distribution and matter profile. To model this effect we take two approaches.

In a first approach, we simply rescale the lensing profile by a mass-independent factor that reads

$$\bar{\kappa}_\ell(M, z) \to \bar{\kappa}_\ell(M, z)\sqrt{\frac{P_{\rm DM+baryons}(k, z)}{P_{\rm DM}(k, z)}}, \tag{10}$$

where $k = (\ell + 1/2)/\chi$, and $P_{\rm DM}$ and $P_{\rm DM+baryons}$ are the power spectrum from a dark-matter-only simulation and the power spectrum from a hydrodynamical simulation with dark-matter and a subgrid prescription for baryonic effects. This approach is equivalent to the one assumed in some cosmic shear analyses, where the effect of baryonic feedback processes is taken into account by rescaling the 3D matter power spectrum [15,21]. When testing the REF, AGN, and AGN 8.5 models, we rescaled the lensing profile using the power spectra measured directly in the corresponding cosmo-OWLs simulations (as reported by van Daalen *et al.* [10]). The effect of the rescaling for the REF model is below 1% at all scales, whereas for the AGN and AGN 8.5 models it mostly dampens the amplitude of $\xi^{\gamma_t y}$ below 10 arc min, reaching a 10% dampening at 2.5 arc min for the AGN 8.5 model (which is the most affected model). For the B12 model we do not have at our disposal the 3D power spectra measured in the corresponding simulations with and without baryonic feedback; so we did not consider this model in this first approach.

In the second approach we model the effects of baryonic feedback on the lensing kernel with more flexibility. Instead of using a rescaled version of the NFW profile, we use the Mead model [57] to determine $u_m(k, M)$, the Fourier transformation of the dark-matter density profile. The Mead model builds upon the NFW

profile, but it adds additional freedom such that the model can capture the effect of baryonic physics on the internal structure of halos. This is achieved by adding two parameters: $A_{\rm Mead}$, the amplitude of the concentration-mass relation, and $\eta_{\rm Mead}$, the "halo bloating parameter," which produces a (mass-dependent) expansion of the halo profile.[4] The NFW profile is still included in the Mead model parameter space, as well as the rescaled versions of the NFW profile used in the aforementioned approach. Full expressions for $u_m(k, M)$ and for the effective linear bias parameter $b_\ell^\kappa(z)$ of the Mead model are provided in paper II. In this second approach, when testing different feedback models, we marginalize over $A_{\rm Mead}$ and $\eta_{\rm Mead}$ using wide priors (similar to the ones assumed by [58]). This is more conservative than rescaling the NFW profile using the power spectra measured in hydrodynamical simulations. Indeed, in the first approach we assumed the rescaling of the lensing kernel to be independent of halo mass; our measurement, however, is mostly sensitive to $M_{200c} \sim 10^{14}\ M_\odot$ (see paper II), so if the effect of baryonic feedback models were halo mass dependent, the rescaling might be not accurate. By marginalizing over the Mead model parameters, we let the data rescale the lensing profile by the "right" amount. Note that *a priori* there should be a relation between the Mead halo model parameters and the pressure profile parameters, as we expect baryonic processes to have a simultaneous impact on the matter and gas. As the Mead halo model implemented in this work is a heuristic model, it is hard to place physically motivated priors on such a relation; therefore, we consider the Mead model and the pressure profile parameters as independent. In this respect, a more coherent frameworks (e.g., [59]) where the shear and TSZ signals are modeled starting from the distribution of gas, matter, and stars can provide better insights into the interplay between the pressure and matter profiles in the presence of baryonic feedback processes.

We provide in Appendix A further validation of our modeling by measuring the shear-Compton-y map cross-correlation on the fiducial DES Y3 N-body simulations.

C. Astrophysical and nuisance parameters

Astrophysical and measurement systematic effects are modeled through nuisance parameters. When performing our analysis, we marginalize over all the nuisance parameters. Values and priors are summarized in Table I.

[4]We note that, in [57], the authors provide best-fit values for the parameters $A_{\rm Mead}$ and $\eta_{\rm Mead}$ for a number of hydrodynamical simulations, as well as suggesting a relation between the two. We cannot use those values or such a relation here, as our implementation of the Mead model is slightly different from the one presented in [57], which is *optimized* for a cosmic shear analysis.

TABLE I. Cosmological, systematic, and astrophysical parameters. The cosmological parameters considered are $\Omega_{\rm m}$, σ_8, $\Omega_{\rm b}$ (the baryonic density in units of the critical density), n_s (the spectral index of primordial density fluctuations), and h (the dimensionless Hubble parameter). The nuisance parameters are the multiplicative shear biases m_i and the photometric uncertainties in the mean of the weak lensing samples Δz_i. The astrophysical parameters $A_{\rm IA,0}$ and $\alpha_{\rm IA}$ describe the intrinsic alignment model, whereas $A_{\rm MEAD}$ and $\eta_{\rm MEAD}$ are the Mead halo model parameters. The column "range" indicates the parameter space spanned when sampling the parameters posterior during the analysis. We report the boundaries for both flat and Gaussian priors. For Gaussian priors we also report the mean and the σ values in the prior column. Priors are described in Sec. III D.

Parameter	Range	Prior
$\Omega_{\rm m}$ (*Planck*)	0.2…0.4	0.315 ± 0.007
σ_8 (*Planck*)	0.6…1.1	0.811 ± 0.006
$\Omega_{\rm m}$ (DES)	0.2…0.4	0.27 ± 0.02
σ_8 (DES)	0.6…1.1	0.82 ± 0.05
h	Fixed	0.674
$n_{\rm s}$	Fixed	0.965
$\Omega_{\rm b}$	Fixed	0.0493
$\Delta m_1 \times 10^2$	−10.0…10.0	-0.63 ± 0.91
$\Delta m_2 \times 10^2$	−10.0…10.0	-1.98 ± 0.78
$\Delta m_3 \times 10^2$	−10.0…10.0	-2.41 ± 0.76
$\Delta m_4 \times 10^2$	−10.0…10.0	-3.69 ± 0.76
$\Delta z_1 \times 10^2$	−10.0…10.0	0.0 ± 1.8
$\Delta z_2 \times 10^2$	−10.0…10.0	0.0 ± 1.5
$\Delta z_3 \times 10^2$	−10.0…10.0	0.0 ± 1.1
$\Delta z_4 \times 10^2$	−10.0…10.0	0.0 ± 1.7
$A_{\rm IA.0}$	−5.0…5.0	0.49 ± 0.15
ηIA	−5.0…5.0	Flat
$A_{\rm MEAD}$	−5.0…5.0	Flat
$\eta_{\rm MEAD}$	0…1.0	Flat

1. Photometric redshift uncertainties

Uncertainties in the photometric redshift estimates from the SOMPZ method for the four tomographic bins of the weak lensing sample are parametrized through a shift Δz in the mean of the redshift distributions,

$$n^i(z) = \hat{n}^i(z - \Delta z), \tag{11}$$

where $\hat{n}^i$ is the original estimate of the redshift distribution coming from the photometric redshift code for the bin i. This parametrization of the redshift uncertainties has shown to be adequate for the DES Y3 analysis [35]. We assume DES Y3 Gaussian priors for the shift parameters.

2. Multiplicative shear biases

Biases coming from the shear measurement pipeline are modeled through an average multiplicative parameter

$1 + m^i$ for each tomographic bin i, which affects our measurement as $\xi^{\gamma_t^i y} \to (1 + m^i)\xi^{\gamma_t^i y}$. Gaussian priors are assumed for each of the m^i and have been estimated in [39]. The major contribution to the shear multiplicative bias comes from blending effects due to source crowding.

3. Intrinsic galaxy alignments

Intrinsic galaxy alignment (IA) has been neglected in all the previous works on shear-Compton-y cross-correlations. In theory, an IA contribution is expected, as Compton-y maps trace the underlying dark-matter density field. Our implementation of the IA model follows the nonlinear alignment model [60,61]. It can be easily incorporated in the modeling by modifying the lensing kernel [Eq. (8)],

$$W^\kappa(\chi) \to W^\kappa(\chi) - A(z(\chi))n_\kappa(z(\chi))\frac{dz}{d\chi}. \tag{12}$$

The amplitude of the IA contribution can be written as a power law,

$$A(z) = A_{\mathrm{IA},0}\left(\frac{1+z}{1+z_0}\right)^{\eta_{\mathrm{IA}}}\frac{c_1\rho_{m,0}}{D(z)}, \tag{13}$$

with $z_0 = 0.62$, $c_1\rho_{m,0} = 0.0134$ [60,62] and $D(z)$ the linear growth factor. We marginalize over $A_{\mathrm{IA},0}$ and η_{IA} assuming the constraints from the DES Y1 3×2 analysis. More details about the IA model and its relative strength compared to the Compton-y-shear signal are given in paper II.

We also tested an additional one-halo IA contribution due to satellite galaxies alignment, following [63]. This extra contribution requires modeling the halo occupation distribution (HOD) of satellite galaxies and the fraction of satellites as a function of redshift, which are somewhat uncertain for the DES Y3 weak lensing sample. For this reason, we decided to remove scales where this extra one-halo model could provide a significant contribution. More details are given in paper II.

D. Likelihood and covariance

Our data vector includes shear-Compton-y map correlations $\xi^{\gamma_t y}$ from both *Planck* and ACT maps. In both cases, we cross-correlated the maps with the four DES Y3 tomographic bins, for a total of eight correlation measurements. We measured the cross-correlations in 20 bins (equally spaced in logarithmic scale) between 2.5 and 250 arc min. We exclude some angular scales from our analysis, based on three different criteria: (1) we exclude all the scales below 8 arc min for the *Planck* measurement, since these scales are well below the *Planck* beam size; (2) we remove small scales where our IA modeling might be inadequate (see paper II); (3) we remove scales that might be significantly affected by CIB contamination (see Sec. IV C). Depending on the tomographic bin, we consider the most stringent criteria among these three. We summarize the scale cuts in Table II. Having defined our data vector, in order to test our models, we evaluate the posterior of the parameters conditional on the data by assuming a multivariate Gaussian likelihood for the data, i.e.,

TABLE II. Angular scales considered for the analysis (in arc min). More details are provided in Sec. III D.

	Bin 1	Bin 2	Bin 3	Bin 4
Planck × DES	20′–250′	8′–250′	8–250	20′–250′
ACT × DES	10′–250′	5′–250′	2.5′–250′	2.5′–250′

$$\ln\mathcal{L}(\boldsymbol{\mathcal{D}}|\Theta) = -\frac{1}{2}(\vec{\boldsymbol{\mathcal{D}}} - \vec{\boldsymbol{\mathcal{T}}}(\Theta))\mathbb{C}^{-1}(\vec{\boldsymbol{\mathcal{D}}} - \vec{\boldsymbol{\mathcal{T}}}(\Theta))^{\mathrm{T}}. \tag{14}$$

Here, $\vec{\boldsymbol{\mathcal{D}}}$ is the measured $\xi_{\gamma_t y}$ data vector of length N_{data}, $\vec{\boldsymbol{\mathcal{T}}}$ is the theoretical model for the data vector at the parameter values given by Θ, and $\mathbb{C}^{-1}$ is the inverse covariance matrix of shape $N_{\mathrm{data}} \times N_{\mathrm{data}}$. The measurement covariance is modeled from theory, including both a Gaussian and a non-Gaussian term; we provide a detailed description in Appendix B, along with validation based on data and simulations. The posterior is then the product of the likelihood and the priors,

$$\mathcal{P}(\Theta|\boldsymbol{\mathcal{D}}) = \frac{\mathcal{L}(\boldsymbol{\mathcal{D}}|\Theta)\mathrm{P}(\Theta)}{\mathrm{P}(\boldsymbol{\mathcal{D}})}, \tag{15}$$

where the $\mathrm{P}(\Theta)$ are the priors on the parameters of our model, and $\mathrm{P}(\boldsymbol{\mathcal{D}})$ is the evidence of data. To sample the posteriors of our parameters, we use the Polychord sampler [64,65], which is a nested sampler that uses slice sampling to sample within the nested isolikelihood contours.

For the cosmological parameters, we assume a flat Λ cold dark matter cosmology and vary two parameters: Ω_{m} and σ_8, leaving Ω_{b} (the baryonic density in units of the critical density), n_s (the spectral index of primordial density fluctuations), and h (the dimensionless Hubble parameter) fixed to values from Planck Collaboration *et al.* [66]. For Ω_{m} and σ_8, and for each model under testing, we run our analysis twice, with Gaussian priors centered in [66] and DES Y1 [67] values, with width equal to the 1σ uncertainty on the two parameters from the two analyses, respectively. We used DES Y1 priors, as at the time of writing the DES Y3 analysis had not been released yet. We also marginalize over nuisance parameters describing photo-z uncertainties, shear biases, and IA effects in our measurements. We use fiducial DES Y3 priors for the photo-z uncertainties and shear biases. As for the IA priors, we use a Gaussian prior on the amplitude of the signal as constrained by the DES Y1 3×2 analysis [68].

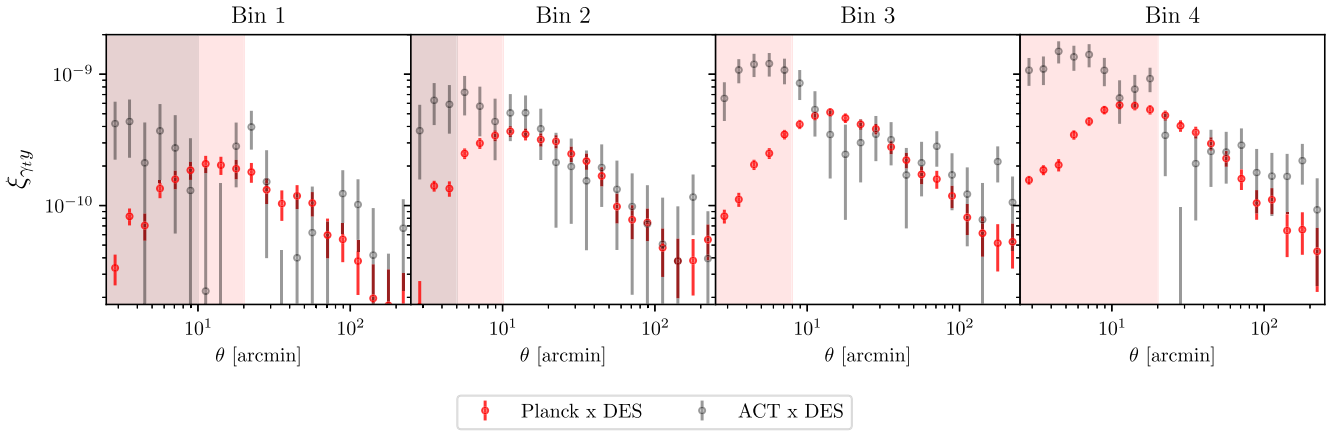

FIG. 5. Measured shear-Compton-y cross-correlation $\xi^{\gamma_t y}$ from data (*Planck* × DES in red ACT × DES in gray). Error bars are taken to be the square root of the diagonal of the theory covariance presented in Appendix B. The edges of the tomographic bins are [0.0, 0.358, 0.631, 0.872, 2.0], although we note that the redshift distributions are not sharply bounded (see Sec. II C). We note that the difference at small scales between the *Planck* and ACT measurement is driven by the different beam size (the *Planck* map has a resolution of 10 arc min, whereas the ACT map has a resolution of 1.6 arc min). The effect of the *Planck* beam becomes negligible above 20 arc min, with the two measurements indeed showing a good agreement at large scales. Red shaded and gray shaded regions represent the scales removed from the main analysis, for the *Planck* × DES and ACT × DES measurements, respectively.

We also marginalize over the Mead halo model parameters $A_{\rm Mead}$ and $\eta_{\rm Mead}$ using broad flat priors.

All the parameters varied in this work and priors assumed are given in Table I. We discuss in detail the impact of the priors on our measurement in Sec. IV D.

IV. RESULTS

We first present our measurement with the relevant systematic tests, and then we show the comparison with the theoretical predictions using the halo model framework and pressure profiles from hydrodynamical simulations.

A. TSZ weak lensing cross-correlation estimator

Our estimator for the TSZ weak lensing cross-correlation is the cross-correlation $\xi^{\gamma_t y}$, which is constructed starting from the DES catalog of galaxy shapes and from the ACT and *Planck* Compton-y maps. Concerning the Compton-y maps, we create a catalog of points using the coordinates of the center of each HEALPY pixel of the maps. For each point we then consider the complex shear of a given galaxy in the DES catalog at an angular separation θ. We then compute the tangential component of the shear and multiply it by the Compton-y value. We average over all the galaxies at that angular separation and over all the points in the Compton-y maps. The DES catalog is divided into four tomographic bins, hence we measure eight correlation functions in total. For the computation of the signal, we use TREECORR [69].

B. Fiducial measurement

Our fiducial measurement, obtained by cross-correlating both the *Planck* and ACT Compton-y maps with the DES shape catalog, is presented in Fig. 5. For the *Planck* map, we used a version of the map where CIB contribution is deprojected (we provide more details in Sec. IV C). From Fig. 4 it can be seen how the *Planck* beam suppresses all the small-scale information, which is retained in the ACT × DES measurement. At large scales the two measurements are consistent with each other, although the ACT × DES measurement is noisier. Since we removed the area from the *Planck* data of the DES footprint covered by ACT, the two datasets can be considered approximately independent. If we select only the large scales unaffected by the beams (e.g., $\theta > 20$ arc min), the two measurements are consistent with each other with a p-value $= 0.05$ ($\chi^2 = 60$ for 44 d.o.f.).[5] As an additional check, we also repeated the measurement using the part of the *Planck* map in the ACT footprint, finding good agreement with the ACT measurement over the same area.

We report in Table III the statistical significance of our measurements. Despite the higher resolution and better small-scale constraints, the ACT × DES measurement delivers lower SNR than *Planck* × DES, due to the smaller sky coverage. The overall SNR for the combined measurement, considering the four tomographic bins together, is nonetheless improved with respect to the *Planck*-only measurement, and it is equal to SNR $= 21$. Concerning the individual tomographic bins, the highest SNR is provided by the correlation with the two tomographic bins with the highest redshift.

[5]We measured the p-value by computing the difference between the two signals and used a theory covariance to estimate the covariance for the measurements' difference.

TABLE III. Measurements' signal-to-noise ratio, defined as SNR $= \sqrt{\chi_{\rm null} - \text{d.o.f.}}$, with $\chi_{\rm null} = \xi^{\gamma_t y} C^{-1} \xi^{\gamma_t y}$. When computing the SNR we exclude scales $\theta < 8$ arc min for the *Planck* measurement, as these scales are significantly smaller than the *Planck* beam.

Bin	*Planck* × DES	ACT × DES	Combined
Bin 1	6.9	3.8	7.9
Bin 2	11	3.2	12
Bin 3	15	6.2	16
Bin 4	15	7.5	17
All bins	19	9.3	21

The effective redshift interval probed by these two correlations is $z \sim 0.3$–0.5 (see paper II). As a comparison, the first measurement of a cross-correlation between a CFHT convergence map and the *Planck* Compton-y map was detected at the $\sim 6\sigma$ C.L. [23]. A stronger detection was achieved by [25], who detected a cross-correlation signal at the $\sim 8.1\sigma$ C.L. for $\xi^{\gamma_t y}$ using *Planck* data and a shape catalog from the RCSLenS survey. Our measurement improves on this, owing to its larger sky coverage of the weak lensing data.

C. CIB contamination and systematic tests

We present here a number of tests to assess whether the Compton-y maps used in this work are affected by systematic effects. In particular, we are interested in the potential effect of two contaminants, namely, the CIB and radio point sources.

The CIB signal is sourced by thermal emission from galaxies over a broad range of redshift ($z \sim 0.1$–4), but with the bulk of the emission mostly peaking at high redshift ($z > 1$, Chiang *et al.* [70], Schmidt *et al.* [71]). By assuming an effective model for the main component of the CIB that is correlated across frequency, the CIB can be deprojected from the Compton-y map using the ILC method [72]. The deprojection is performed at the map-making level, once a frequency dependence for the Compton-y and CIB signals have been assumed. When coadding maps from different frequency channels, weights are assigned to each channel such that the coadded map has minimum variance, unit response to the Compton-y signal, and null response to the CIB signal. The particular implementation adopted for the *Planck* maps is described in [35], whereas the implementation adopted in the ACT maps is described in [29]. The deprojection procedure introduces some additional noise into the maps, which is properly accounted for in our covariance matrix.

We model the effective CIB spectral energy distribution (SED) as a modified blackbody with "temperature" 24 K and spectral index β (following [29]). The parameters of this effective model do not correspond to the physical SED parameters of an actual infrared source, but they do capture the frequency dependence seen in the sky-average CIB SED for the CIB halo model fit to the *Planck* CIB power spectra measurements. In this model the CIB emission rises quickly at high frequency and it is expected to mostly affect the frequency channel at 545 GHz. We create three Compton-y maps using *Planck* frequency channels from 30 to 545 GHz, deprojecting the CIB assuming the SED from [29] with slope $\beta = 1.0,\ 1.2,\ 1.4$.[6] In what follows, whenever needed, we will assume the value $\beta = 1.2$ and show the results for values $\beta = 1.0,\ 1.4$ only for comparison purposes. The value $\beta = 1.2$ is the one assumed in [29], obtained by comparison with the *Planck* CIB halo model presented in [73]. The shear-Compton-y cross-correlation $\xi^{\gamma_t y}$ signal obtained using these maps is shown in Fig. 6, compared to the measurement obtained using the official *Planck* NILC Compton-y map presented in [28], which does not implement any CIB deprojection. Bins 3 and 4 are the ones where the measured signal is mostly affected by the CIB deprojection procedure, depending on the value of the SED slope β. We can quantify the effect of the CIB deprojection by measuring the significance of the difference between the signal obtained using the official *Planck* map and our deprojected maps. To this aim, we use a jackknife [74,75] covariance (see Appendix B) for the measurement difference and restrict to the scales where the jackknife estimate is not affected by the limited size of the jackknife patches ($\theta < 40$ arc min in this case). We note that such a covariance is smaller than the measurement covariance, because sample variance should largely cancel when computing the difference between two signals measured over the same area.

This procedure is needed as the measurements involving the maps with and without CIB deprojections are highly correlated. When assuming $\beta = 1.2$, the χ^2 of the difference between the signals is $\chi^2 = 4, \chi^2 = 12, \chi^2 = 55, \chi^2 = 110$ for 8 d.o.f. for the four tomographic bins, respectively (Table IV). We further generate three additional *Planck* maps removing the 545 GHz frequency channel and assuming again $\beta = 1.0,\ 1.2,\ 1.4$. These are generally compatible with the ones including it (although they are noisier), except for the scales between 8 and 20 arc min in bin 4 (middle panels of Fig. 6). Given these results, for the analysis presented in this work we decide to rely on the *Planck* Compton-y map obtained using all the frequency channels from 30 to 545 GHz and with CIB deprojected using $\beta = 1.2$ for the CIB SED. We further decide to exclude in bin 4 scales $\theta < 20$ arc min, due to potential residual CIB contamination. Note that previous work on

[6]We also tried with a larger value of $\beta = 1.6$, but found significantly increased uncertainties and no appreciable difference with respect to $\beta = 1.4$. This happens because $\beta = 1.6$ is a large value which does not describe well the data, and as a consequence, the CIB deprojection does not work properly.

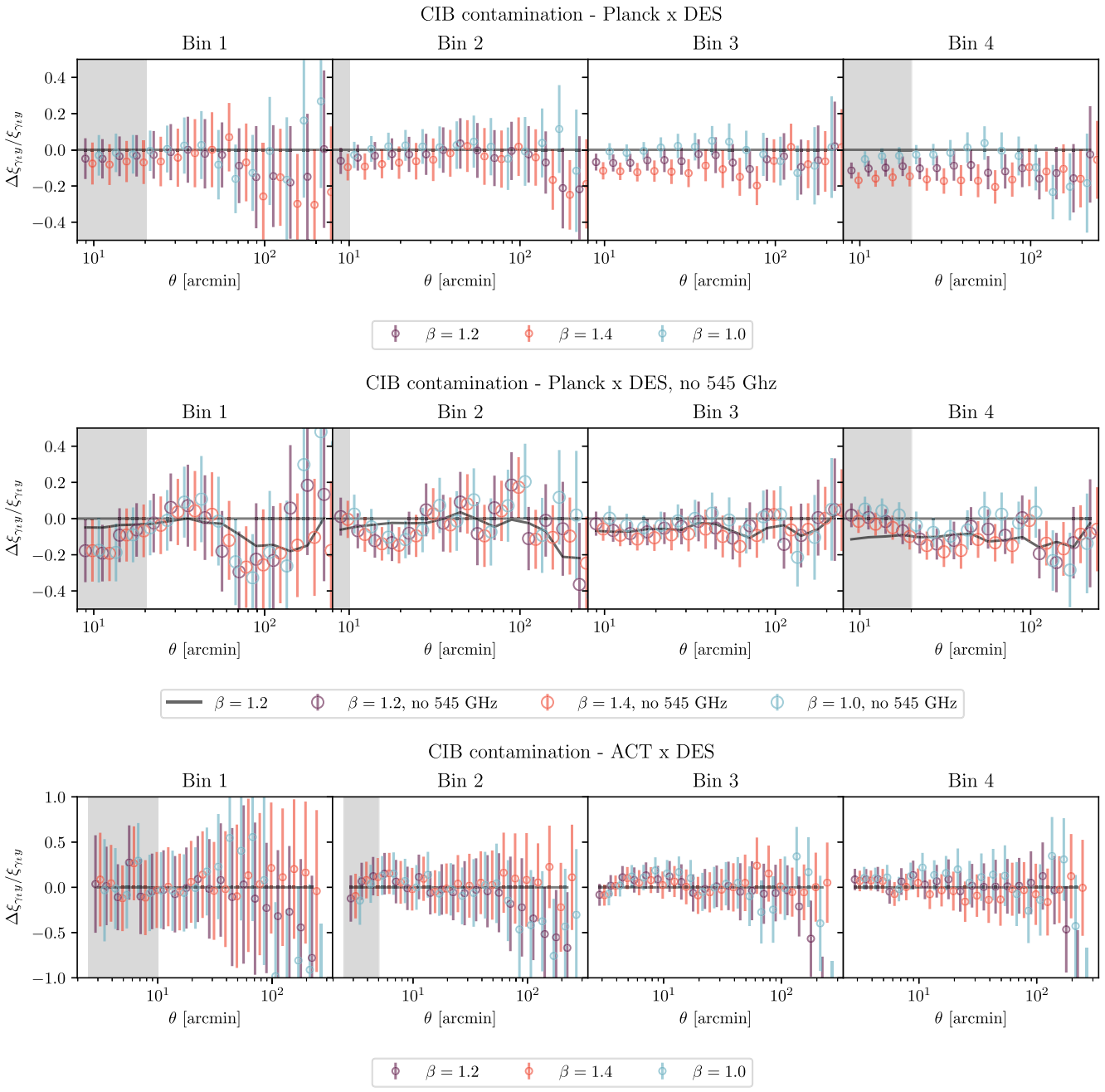

FIG. 6. Fractional difference in the measured shear-Compton-y cross-correlation $\xi^{\gamma_t y}$ when computed using the Compton-y map after deprojecting the CIB component, with respect to the map with no CIB deprojection. The upper plots show the results for the *Planck* maps created using all the frequency channels between 30 and 545 GHz; the central plots show the results for the *Planck* maps excluding the 545 GHz frequency channel. In the central panels, the solid black line shows the $\beta = 1.2$ measurement when including the 545 GHz channel (from the upper panel plots) as a comparison. CIB has a strong impact on the *Planck* × DES measurements, especially for the ones involving the two highest redshift bins (see upper panel). CIB contamination is also seen when removing the 545 GHz frequency channel (central panels). The lower panels show the results for the ACT maps, which indicates negligible CIB contamination. Gray shaded regions represent the scales removed from the main analysis. The data are strongly correlated (adjacent bins are 60%–80% correlated, see Fig. 12 of paper II).

shear-Compton-y cross-correlation using the *Planck* Compton-y map suggested a weaker level of CIB contamination [76]. It is possible that the different redshift distribution of the galaxies used in this work could be responsible for a higher degree of CIB contamination compared to the work of [76], in particular, the redshift distributions of our bin 3 and 4 peak at higher redshift with respect to the sample used in [76], overlapping more with

TABLE IV. Summary of the compatibility and systematic tests performed on our measurements. We report the χ^2 and the d.o.f. for the difference between the *Planck* and ACT measurements, as well as the difference between the measurements obtained using CIB deprojected maps and without deprojection. Last, for the $\gamma_\times$ test we report the χ^2 of the null hypothesis (i.e., no signal). The number of d.o.f varies depending on whether the covariance is a theory covariance (which is the case of *Planck*-ACT compatibility) or a jackknife covariance (all the other cases), since for the latter case only the scales where the covariances is reliable have been used.

Test	χ^2/d.o.f.
Planck-ACT compatibility, all bins	60/44
Planck × CIB, bin 1	4/8
Planck × CIB, bin 2	12/8
Planck × CIB, bin 3	55/8
Planck × CIB, bin 4	110/8
ACT × CIB, bin 1	4/8
ACT × CIB, bin 2	8/8
ACT × CIB, bin 3	14/8
ACT × CIB, bin 4	9/8
Planck radio contamination	34/32
Planck, $\gamma_\times$, all bins	84/68
ACT, $\gamma_\times$, all bins	93/80

the high redshift galaxies responsible for the bulk of the CIB emission. Additional discussion on the effects of CIB contamination using simulated Compton-y maps are provided in Appendix C. Last, we also show in Fig. 6 the effect of CIB deprojection on the cross-correlation $\xi^{\gamma_t y}$ signal obtained using the ACT maps. The effect is negligible here, as the χ^2 of the signal's difference is compatible with noise: we obtain $\chi^2 = 4$, $\chi^2 = 8$, $\chi^2 = 14$, $\chi^2 = 9$ for 8 d.o.f, for scales $\theta < 15$ arc min, for the four tomographic bins (Table IV).[7] This is due to the ACT measurement being noisier than *Planck* (due to the smaller area coverage) and due to the ACT Compton-y map receiving significant contributions from the ACT 98 and 150 GHz channels (even on small scales), where the CIB is relatively faint. We also note that [77] found some evidence of mild CIB contamination for the ACT map only at scales smaller than 1 arc min, which are scales not considered in this work. Given the result of this test, in what follows, we will use the ACT map with no CIB deprojection.

As a second test, we proceed testing the potential contamination due to radio sources. Radio sources can potentially bias the signal at the 10%–20% level [78], although the exact number depends on the SED and HOD of the radio sources, which are uncertain, and on the map-making algorithm. Due to the uncertainties in the SED and HOD, the radio sources' contamination cannot be as easily deprojected as the CIB signal. The ACT map is created masking detected radio sources in every channel, and subsequently interpolating the map over the masked regions [29]; radio sources are usually detected down to 5–10 mJy. On the other hand, the *Planck* map used in this work does not have any radio sources mask applied by default. We therefore apply a radio sources mask to the *Planck* Compton-y map, using a catalog of radio sources detected by ACT at 98 and 150 GHz. Such a catalog has not been released yet; it is built using ACT DR5 data and spans the full DES Y3 footprint [50]. Note that ACT can detect pointlike radio sources much fainter than *Planck* (1–2 orders of magnitude fainter, depending on the *Planck* channel considered, Planck Collaboration *et al.* [79]). We masked a circular area of radius 10 arc min around each source and repeated the cross-correlation measurement with the DES shape catalog. The masking reduced by 8% the area available for the cross-correlation. The difference in the measurements (with and without radio sources mask applied) is shown in Fig. 7. No radio source signal is detected in the measurements' difference: using the angular scales where the jackknife covariance is reliable, we obtained for the difference between the two signals χ^2/d.o.f. = 34/32, see Table IV. Given the lower signal-to-noise ratio of the ACT measurement, and given the fact that this radio sources mask is already applied to the ACT map, we can also consider the impact of radio sources on the ACT map negligible.

As a last systematic test, we checked the cross-component of the mean shear around every point of the Compton-y maps. The cross-component is a standard null test in galaxy-galaxy lensing studies, as it should be compatible with zero if the shear is produced by gravitational lensing alone. The cross-component should also vanish in the presence of systematic effects that are invariant under parity. We test this in Fig. 8. Using a theory covariance, we obtain χ^2/d.o.f. = 84/68 and χ^2/d.o.f. = 93/80 for the *Planck* × DES and ACT × DES measurements (Table IV), respectively, indicating compatibility with a null signal and that the null test is passed.

D. Tests of feedback models

After characterizing the measurement, we compare it to theoretical predictions using the halo model framework and pressure profiles as estimated from a number of hydrodynamical simulations. The pressure profiles and feedback models considered in this section are the five models introduced in Sec. III A (B12, REF, AGN, AGN8.5, TNG). For the lensing part of the signal, we both model our theoretical predictions using the rescaled NFW profiles and using the Mead model (Sec. III B). We compare our

[7]These χ^2 values are computed using as a covariance the measurements' difference covariance, which is smaller than the covariance of a single measurement due to canceling sample variance. As a reference, if we were to compute the χ^2 of the signals difference using the single measurement covariance, we would obtain $\chi^2 \sim 2$–$3/8$ d.o.f.

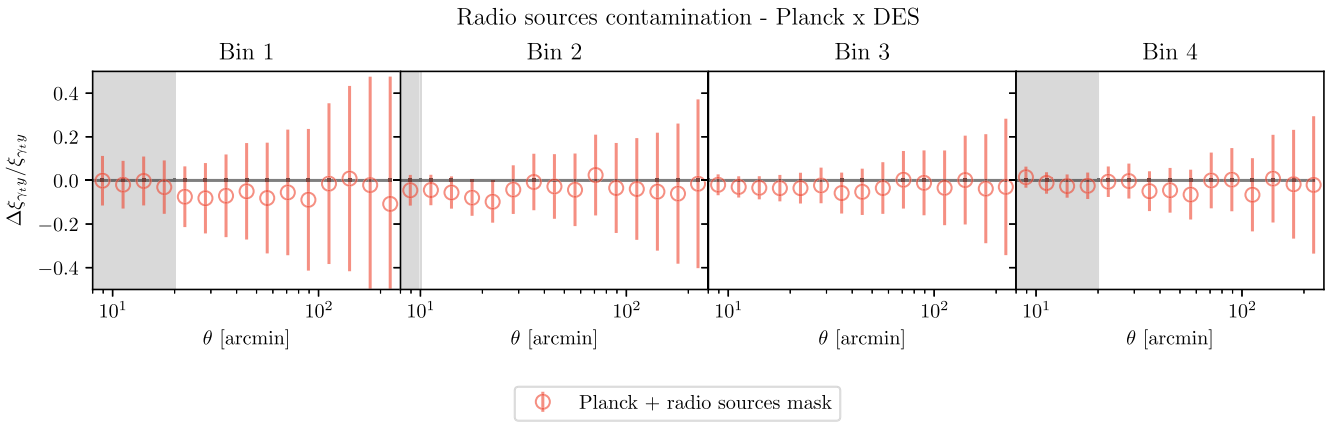

FIG. 7. Fractional difference in the measured shear-Compton-y cross-correlation $\xi^{\gamma_t y}$ when computed using the *Planck* Compton-y map with and without masking radio sources. No statistically significant difference is measured, indicating no contamination due to radio sources. Gray shaded regions represent the scales removed in the main analysis.

theoretical models to the measurement marginalizing over a number of nuisance parameters modeling astrophysical and measurement systematics, including photometric redshift uncertainties, intrinsic alignment, and shear calibration biases, as described in Sec. III D. We also marginalize over σ_8 and Ω_m assuming *Planck* priors for the cosmological parameters (but we also repeat the analysis in Appendix D using DES Y1 priors). Such marginalization over systematics has generally been neglected in early works on weak lensing–TSZ correlations (but see Osato *et al.* [26]). When comparing models to the measurements, we always jointly fit the ACT × DES and *Planck* × DES measurements.

We start considering the analysis with rescaled NFW profiles for the lensing part of the signal. This is the most constraining setup, as we do not marginalize over the effect of baryonic feedback on the matter profile, but rather we rely on the measurements of power spectra from hydrodynamic simulations to rescale our theoretical predictions of the matter profile. Note that such rescaling has a milder impact on the measurement compared to the effect of differences in the pressure profile from different hydrodynamical simulations. The main caveat of this approach is that such rescaling neglects any halo mass dependency of the effect of baryonic feedback on the matter profile, as the power spectra do not carry information about the halo mass, so it can be seen as an "effective" rescaling. Note that due to the lack of the 3D power spectrum needed for the rescaling for the B12 model, we did not consider it in this first part of the analysis.

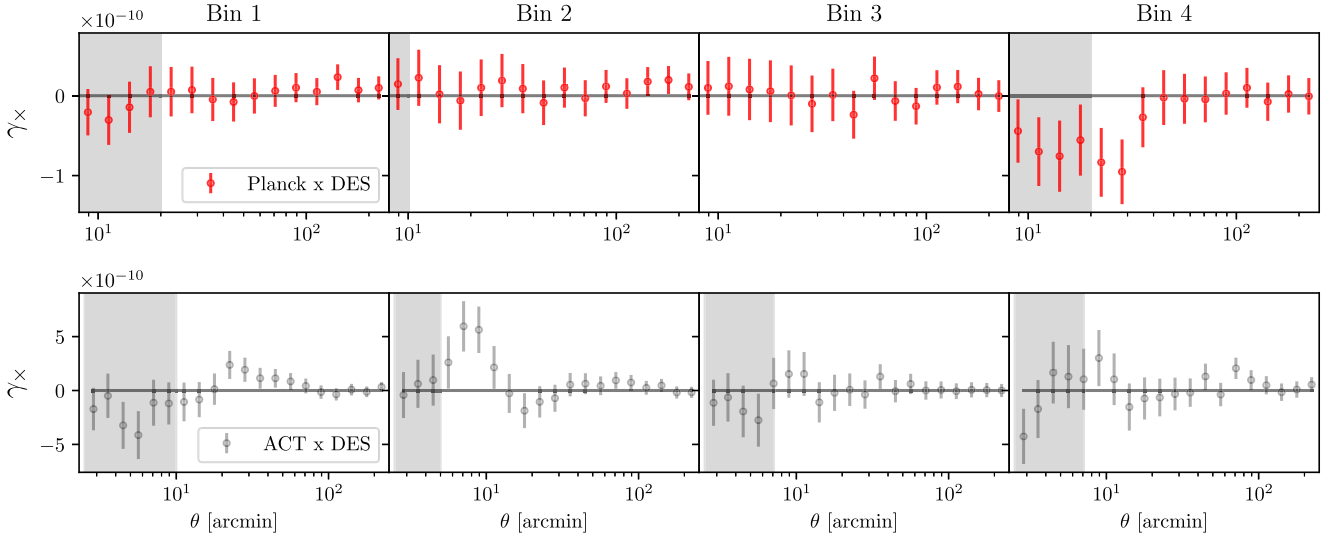

FIG. 8. Cross-component of the lensing signal around points of the Compton-y maps. Gray shaded regions represent the scales removed in the main analysis. No statistically significant signal is measured (Table IV), indicating that the null test is passed. We note that the few points at ∼10 arc min for the second bin of the ACT × DES measurement that are showing a small deviation from zero are very correlated and are just a statistical fluke (we also tried to change the binning of the measurement, finding again a null signal).

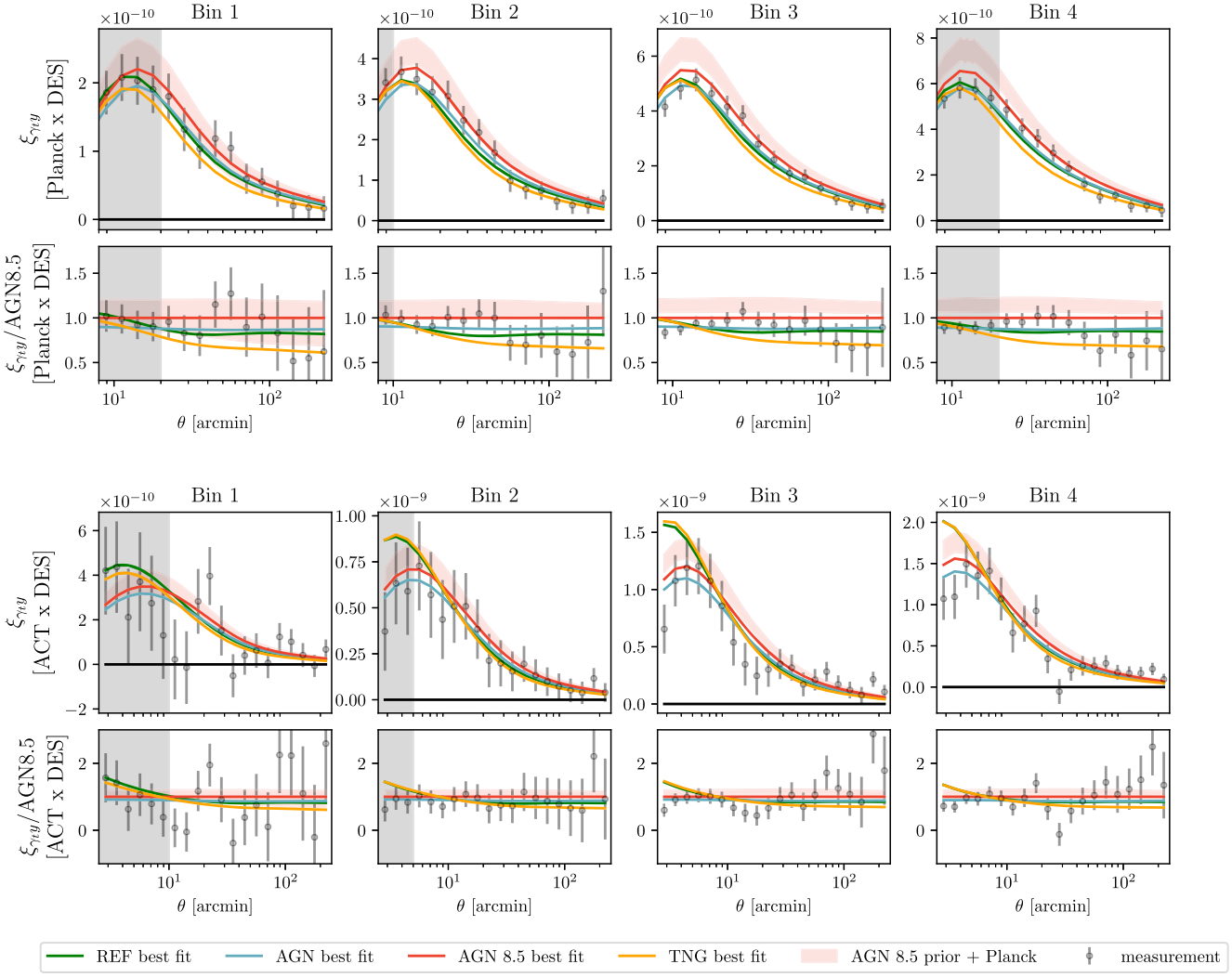

FIG. 9. Measured shear-Compton-y cross-correlation $\xi^{\gamma_t y}$ and best-fit models for four feedback models (TNG, AGN, AGN8.5, and REF). These models have been obtained assuming the rescaled NFW profile for the lensing signal. Top panels show the cross-correlations between *Planck* and DES Y3 data for the four tomographic bins, whereas bottom panels show the correlations between ACT and DES Y3 data. As a comparison, we also show as a colored band encompassing the 68% confidence interval of the prior for the AGN 8.5 scenario. The gray shaded regions represent the angular scales not included in our analysis (see Table II).

Figure 9 shows the maximum *a posteriori* (MAP) models obtained by assuming the four feedback models and marginalizing over nuisance and cosmological parameters. The pressure profiles are not varied, only the nuisance and cosmological parameters; so the best-fit models for our measurements are obtained using the pressure profiles from the hydrodynamical simulations and the best-fit nuisance and cosmological parameters from the analysis. The data likelihood at MAP is approximately described as a χ^2 distribution with d.o.f. equal to the number of data points $N_{\rm points}$ minus the effective number of parameters $N_{\rm eff}$ constrained by our data compared to the priors it began with [80]. In our case $N_{\rm points} = 123$, whereas the effective number is

$$N_{\rm eff} = N - {\rm tr}[(\mathcal{C}^{\rm p})^{-1}\mathcal{C}^{\rm p+d}], \tag{16}$$

where $\mathcal{C}^{\rm p}$ is the covariance of the prior, and $\mathcal{C}^{\rm p+d}$ is the covariance of the prior updated by the data (i.e., the posterior). Moreover, $N = 12$, that is, the number of free 12 parameters in our analysis. We obtain, depending on the model, $N_{\rm eff} \sim 4$. We note that, although we free 12 parameters in our analysis, some of them are tightly constrained by their prior, such that $N_{\rm eff} < 12$. The data likelihood at MAP is reported in Table V. The model that provides the MAP best fit χ^2 is the AGN 8.5 model, followed by the AGN 8, REF, and the TNG model. In particular, the last two feedback models are penalized by the comparison with the ACT × DES data, which prefer the scenarios with a lower amplitude of the pressure profile at small scales, compatible with the ejection of gas from the inner part of the halo. On the other hand, the AGN 8.5 model also provides a better fit to the *Planck* × DES measurement at all scales (especially for bins

3 and 4) compared to the AGN model, hence providing the best χ^2 among all the scenarios probed here.

We compare if the best-fit models are in tension with their priors. In order to quantify the level of agreement/disagreement we use a Gaussian estimator, called update-difference-in-mean statistic [80]. The UDM statistics compare the mean parameters from the prior $\hat{\theta}^{\rm p}$ with the updated values $\hat{\theta}^{\rm p+d}$ obtained running the analysis on data. This statistic assumes either flat or Gaussian priors (which is satisfied for all the parameters considered in this analysis, see Table I) and requires the posterior of the well-constrained parameters to be approximately Gaussian (which is also satisfied). In particular, we can define

$$Q_{\rm UDM} = (\hat{\theta}^{\rm p+d} - \hat{\theta}^{\rm p})^T (\mathcal{C}^{\rm p} - \mathcal{C}^{\rm p+d})^{-1} (\hat{\theta}^{\rm p+d} - \hat{\theta}^{\rm p}), \quad (17)$$

where the difference in the mean of the parameters $(\hat{\theta}^{\rm p+d} - \hat{\theta}^{\rm p})$ is weighted by the parameters inverse covariance. If the parameters are Gaussian distributed, $Q_{\rm UDM}$ is chi-squared distributed with $\mathrm{rank}(\mathcal{C}^{\rm p+d} - \mathcal{C}^{\rm p})$ degrees of freedom. The UDM tension is reported in Table V. A tension would imply that, for a *Planck* cosmological model, the TSZ signal that we measure is in tension with the predictions of these feedback models. For the AGN, REF, and TNG models, the best fits are in tension at the 3–4σ level with their priors, with the best-fit models to the data preferring different values of the cosmological parameters σ_8 and $\Omega_{\rm m}$ than the ones measured by *Planck*. This is also shown in Fig. 10, which reports the posterior of the σ_8 and $\Omega_{\rm m}$ parameters, compared to the priors used in the analysis.[8] On the other hand, the AGN 8.5 scenario, which is also the one that provides the best fit to the data, is not in significant tension with its prior. Given the fact that the AGN 8.5 scenario is also the one that provides the best-fit χ^2, this reinforces the idea that the data prefer a model with a low amplitude of the pressure profile at small scales.

We then repeat the analysis using the Mead model for the lensing signal, instead of using the rescaled NFW profiles. This approach is more conservative, as we let the data rescale the lensing profile instead of relying on the power spectra measured on simulations. This approach is, however, less constraining, as we marginalize over the Mead model parameters using wide priors. In this case all the models provide a similar best fit χ^2. The fact that the best fit of all the different feedback models are similar is related to the large, uninformative prior on the Mead model parameters, which, together with the freedom allowed by the priors on the cosmological and nuisance parameters, absorbs most of the differences between models. Interestingly, the best fit χ^2 of all the models obtained freeing Mead model parameters is not too different from the best fit χ^2 obtained for the AGN 8.5 model and rescaling the NFW profile.

TABLE V. The MAP value of χ^2 for the feedback models, obtained assuming *Planck* priors on σ_8 and $\Omega_{\rm m}$, and marginalizing over nuisance parameters as explained in Sec. III D. The top half of the table refers to the models obtained rescaling the NFW profile for the lensing signal; on the other hand, the bottom half of the table refers to the analysis where we model the lensing signal using the Mead model. We also report the update-difference-in-mean (UDM) tension for the best-fit models with respect to their priors.

Planck prior (NFW rescaling)					
	B12	AGN	AGN 8.5	REF	TNG
χ^2/d.o.f.	⋯	172/119	158/119	189/119	198/119
UDM tension	⋯	4.5σ	2.2σ	3.3σ	4.3σ
Planck prior (free $A_{\rm Mead}$, $\eta_{\rm Mead}$)					
	B12	AGN	AGN 8.5	REF	TNG
χ^2/d.o.f.	154/118	155/118	154/118	155/118	154/118
UDM tension	0.7σ	1.5σ	1.4σ	0.5σ	0.3σ

We show in Fig. 11 the posterior of the Mead model parameters for each of the feedback models. In general, the feedback models prefer smaller $A_{\rm Mead}$ and larger $\eta_{\rm Mead}$ than the NFW profile (except for the $A_{\rm Mead}$ parameter for the AGN 8.5 feedback model), which implies less concentrated and more "bloated" halos. Last, we note that the UDM statistics for this second analysis is not in tension with the *Planck* prior (Fig. 10 and Table V), owing to a larger prior space.

We test whether our findings are robust against the exact value of the parameter β used to deproject the CIB contribution in the *Planck* map. To test this, we ran a full analysis using the measurements without CIB deprojection for the *Planck* × DES measurement. This is an extreme case, as we believe the CIB deprojection is necessary, and the value $\beta = 1.2$ used in the fiducial analysis is justified by [29]. Nonetheless, we confirm that, also in this unrealistic case, when running using the rescaled NFW profiles the data prefer the AGN 8.5 model in terms of best fit χ^2. We find, however, that the UDM tension metric increases for all the models[9]: neglecting the CIB deprojection makes our analysis prefer a different cosmology than *Planck*, but it does not have an impact on the feedback model selection.

[8] We caution the reader from "reading" the exact value of the UDM tension from Fig. 10: the posteriors are the results of the combination of the *Planck* prior and the feedback models' likelihood, whereas the UDM tension computes the tension between the model *alone* and the prior, which is in general larger than what it could be inferred "by-eye" from Fig. 10.

[9] In particular, when assuming NFW rescaling we obtain a UDM tension of 6.3σ, 3.8σ, 5.2σ, 6.1σ for the AGN, AGN 8.5, REF, and TNG models, respectively. The UDM tension increases also when the Mead model is assumed: 2.3σ, 2.6σ, 1.2σ, 1.4σ, 2.0σ for the AGN, AGN 8.5, REF, TNG, and B12 models, respectively.

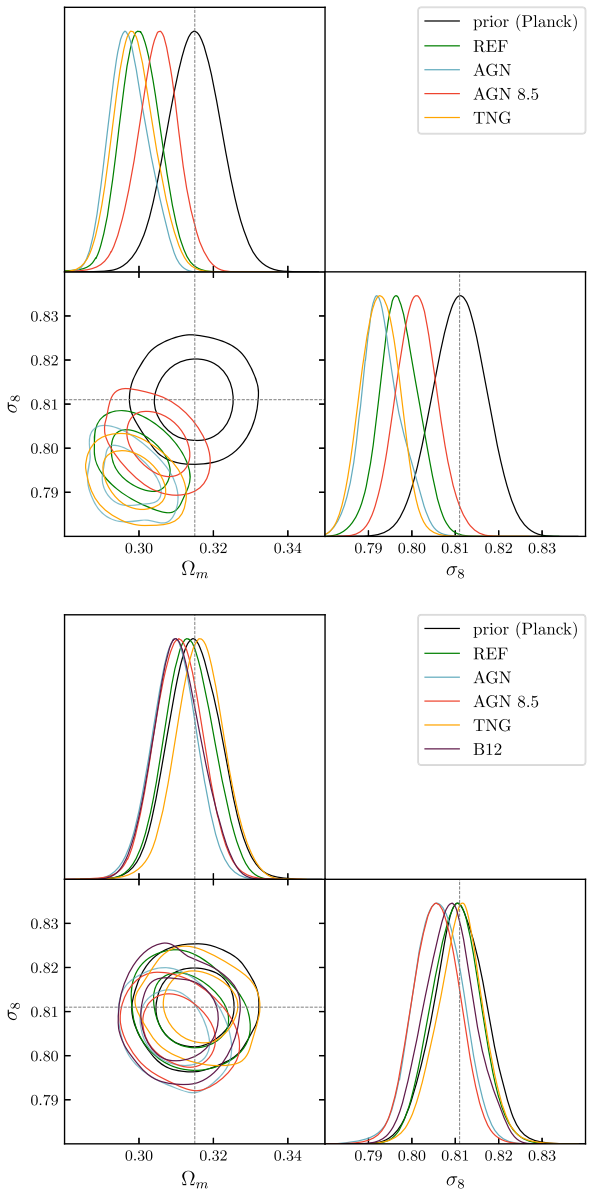

FIG. 10. Posterior for the parameters σ_8 and Ω_m for the four (five) feedback models: (B12), REF, AGN, AGN 8.5, and TNG. We also show the *Planck* prior centered in each plot. Top refers to the case where we used the NFW rescaling to model the lensing part of our signal; the bottom plot refers to the more conservative analysis where we used the Mead model. The marginalized contours in these figures show the 68% and 95% confidence levels. When the NFW rescaling is used, the data are in mild to moderate tension with the *Planck* prior (2.2σ–4.5σ, see Table V).

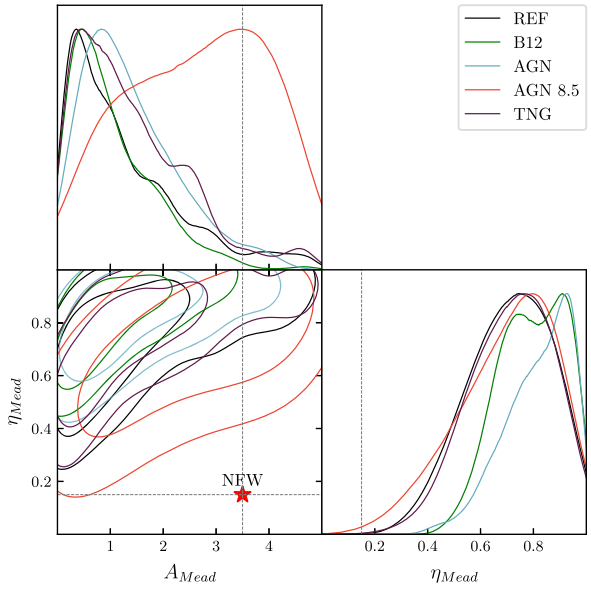

FIG. 11. Posterior for the Mead model parameters $A_{\rm Mead}$ and $\eta_{\rm Mead}$ for five feedback models: B12, REF, AGN, AGN 8.5, and TNG. The "star" indicates the values of the Mead models that best describes a NFW profile. The marginalized contours in this figure shows the 68% and 95% confidence levels.

Finally, we investigate the limitation in our ability to constrain different feedback models due to our measurement uncertainties and lack of tight priors on our nuisance parameters. This is shown in Fig. 12. The colored bands show the contribution of each single nuisance parameter to the total 68% confidence interval of our prior. Note that we assumed the *Planck* prior for σ_8 and $\Omega_{\rm m}$. Quantities in Fig. 12 are shown with respect to a theory data vector obtained assuming the AGN8.5 model. We also show in the plot the fractional difference (in absolute value) with respect to two other feedback models (AGN, REF).

For the purposes of feedback model selection, the ideal situation would be a regime where differences between models are larger than measurement uncertainties (black lines) (and that measurement uncertainties are not subdominant with respect to the prior). This is not happening with our current data: our measurement uncertainties are generally larger than the difference between the models, except for a small window at ∼10–20 arc min in bins 3 and 4 for the Planck × DES measurement and small scales (<5 arc min) in bins 3 and 4 for the ACT × DES measurement. Our measurement uncertainties scale linearly with the inverse of the area covered by our data; moreover, we are still far from the sample-variance limit, with Compton-y noise and shape noise contributing significantly (and similarly) to the error budget. The measurements are completely dominated by noise at small scales, while at large scales cosmic variance becomes more important. For example, reducing Compton-y noise or shape noise by 50% would translate into a ∼50% (20%) change in the amplitude of the diagonal elements of the covariance matrix at 2.5 (250) arc min. This means that our analysis will become significantly more constraining with future datasets. In this respect, future releases of the ACT Compton-y map [81] will definitely improve the situation. The next ACT Compton-y map will cover the full DES Y3 footprint. This means that our measurement uncertainties from the ACT × DES correlations will be significantly smaller compared to the ones shown in this paper—as a comparison, they should be smaller than the ones

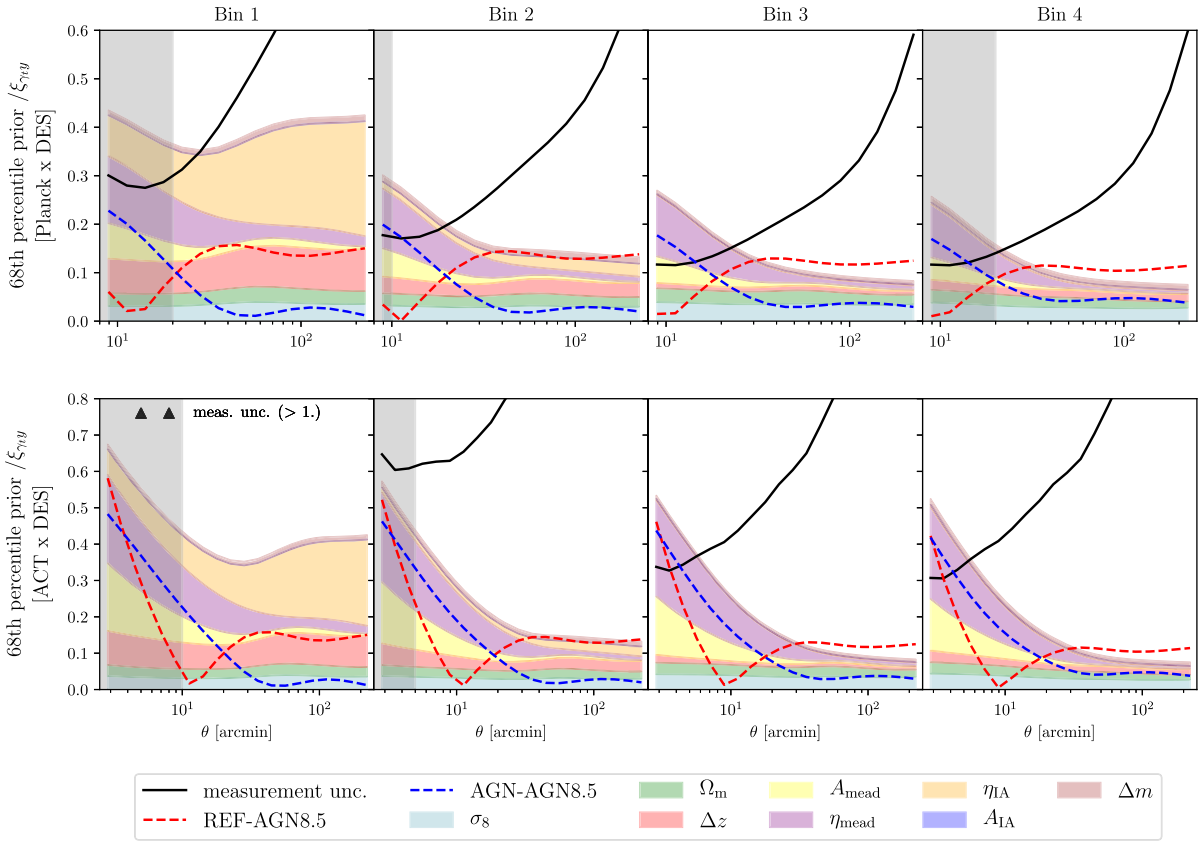

FIG. 12. The plot assesses how our ability to discriminate among different feedback models is limited by our measurement uncertainties and nuisance parameters. In particular, the colored bands show the contribution of each single nuisance parameter to the total 68% confidence interval of our prior. We assume *Planck* priors for σ_8 and Ω_m. The black line represents the measurement uncertainty. The vertical gray line indicates the scale cut adopted in this analysis (Table II). Quantities in the figure are divided by a theory data vector $\xi^{\gamma_t y}$ obtained for the AGN8.5 feedback model. We also show the fractional difference with respect to two other models: REF and AGN. Areas where the black line is below the combined prior budget can be used to differentiate between models.

quoted for *Planck* × DES in Fig. 12 (as in this work we removed a part of the *Planck* data), with the measurement extending down to small scales (∼2.5 arc min). The expected SNR of the new measurement should be around SNR ∼ 27, with measurement uncertainties significantly smaller than the differences between different AGN feedback models (see Fig. 13). The upcoming DES Y6 shape catalog will double the number density of the galaxies compared to the DES Y3 catalog; if used in combination with the new ACT map, we anticipate an improved SNR ∼ 33 and also an improved sensitivity to different feedback models (Fig. 13). Of course, if the confidence interval spanned by the prior is still larger than the difference between models, the increased constraining power will mostly constrain the nuisance parameters; hence it is important to add additional information to reduce the impact of large priors on our analysis.

In Fig. 12 we note the large contribution of the Mead model nuisance parameters to the 68% confidence interval of the prior. This is a substantial contribution that dominates the prior at scales <20 arc min, and it explains why when marginalizing over Mead model parameters our data could not discriminate among feedback models. At low redshift, uncertainties in the redshift estimates and intrinsic alignment parameter η_{IA} are also providing a substantial contribution (note that A_{IA} is instead tightly constrained by the prior, so it has a negligible impact and its 68% confidence interval cannot be seen in Fig. 12). This is expected, as the lensing signal is smaller in amplitude at low redshift compared to higher redshift, and uncertainties on intrinsic alignment or redshift estimates can have a larger impact. In principle, one could estimate the correct values of the Mead parameters A_{Mead} and η_{Mead} measuring the matter profiles in hydrodynamical simulations for the range of halo masses our measurement is sensitive to (which should be more accurate than just rescaling the NFW profiles). Additional constraints on the Mead model parameters can be provided by a joint analysis with cosmic shear, including small scales (although cosmic shear is sensitive to lower mass halos compared to $\xi^{\gamma_t y}$). When varying Mead model parameters, we are not assuming any prior on the relation with the pressure profiles parameters; in principle, however, the two might be related. As we mentioned in Sec. III B, since our

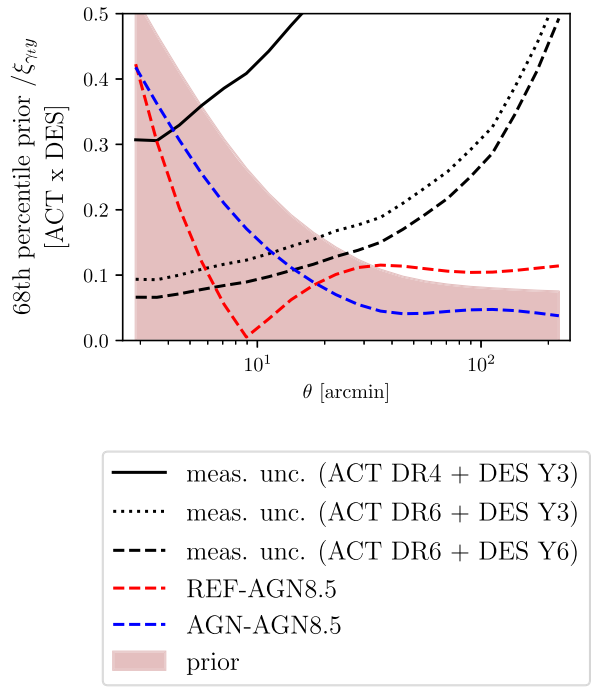

FIG. 13. Same as Fig. 12, but only for the fourth tomographic bin and for three different measurement uncertainties: (1) a black solid line representing the uncertainties from the ACT map × DES Y3 shape catalog used in this paper; (2) a dotted line, obtained assuming the upcoming ACT Compton-y map [81] and the DES Y3 catalog; (3) a dashed line, where the new ACT map and the upcoming DES Y6 number density have been assumed. The magenta shaded region represents the 68% confidence interval of our prior.

Mead model is an effective model, it is hard to place physically motivated priors on the relation between the pressure profile parameters and the Mead model parameters. A joint cosmic shear and TSZ shear analysis would benefit from having physically motivated priors relating the two sets of parameters, as this would help tighten the constraints. In this respect, more coherent frameworks (as the one introduced in Mead *et al.* [59]) where the shear and TSZ signals are modeled starting from the distribution of gas, matter, and stars, might be better suited to this task. Future analysis should also improve the modeling of intrinsic alignment; in this work we took a conservative approach and we removed a good portion of angular scales from the two lowest redshift bins due to the uncertainties in the modeling of the one-halo IA contribution due to satellite galaxies alignment. A joint analysis with cosmic shear, with better IA modeling on small scales, could allow us to also use the smallest scales of our measurements at low redshift, with tighter constraints on IA nuisance parameters.

V. SUMMARY

This is the first of two works on cross-correlations between thermal Sunyaev-Zel'dovich maps from *Planck* and the Atacama Cosmology Telescope and weak gravitational lensing shears measured during the first three years of observations of the Dark Energy Survey. This correlation is sensitive to the thermal energy in baryons as a function of redshift and is, in principle, a powerful probe of astrophysical feedback. In this work we presented the cross-correlation measurements: we detected the correlation at a significance of 21σ, the highest significance to date. We also presented a series of systematic tests, where we tested the effect of potential contaminants on our measurements, including CIB and radio sources. We found that CIB has a substantial effect on the *Planck* × DES measurement, whereas the ACT × DES measurement was not significantly affected, probably due to the ACT Compton-y map receiving significant contributions from the ACT 98 and 150 GHz channels, where the CIB is relatively faint, and also due to the noisier nature of the latter measurement. In order to account for the CIB effect, we built a CIB deprojected Compton-y map for the *Planck* data and used it in our main analysis.

We then used the shear-y correlation measurements to test a number of different feedback models, modeling the correlations using the halo model formalism. In particular, we modeled the TSZ part of the signal using a number of different pressure profiles calibrated against hydrodynamical simulation which have implemented different baryonic feedback models. On the other hand, the shear part was modeled either using a rescaled NFW profile or implementing the Mead halo model [57]. In the first approach, the NFW profile was rescaled by a mass-independent factor given by the ratio of the power spectrum from a dark-matter-only simulation and the power spectrum from a hydrodynamical simulation with dark-matter and a subgrid prescription for baryonic effects. In the second approach, the lensing kernel was modeled by a generalized NFW profile [57] with extra degrees of freedom to take into account the effect of baryonic feedback processes. When comparing our models to our measurement, we kept the pressure profile model fixed, as our goal was to discriminate among different feedback models. Note that a different approach where the pressure profile parameters are varied is adopted in paper II.

In our analysis, we marginalized over ten nuisance parameters capturing redshift uncertainties, shear calibration biases, and intrinsic alignment effects adopting DES priors. We also marginalized over Ω_m and σ_8 using *Planck* and DES priors, and when used, over the Mead halo model parameters. We found when using the rescaled NFW profile in combination with the pressure profiles from hydrodynamical simulations, the data preferred a lower amplitude of the pressure profile at small scales, compatible with a scenario with stronger AGN feedback and ejection of gas from the inner part of the halos (the AGN 8.5 model). We quantified the level of agreement/disagreement of each model with the data using Gaussian estimators [80], and we

found that, when assuming *Planck* priors on the cosmological parameters Ω_m and σ_8, all the models were in 3–4σ tension with the prior, except for the AGN 8.5 model, which showed a lower tension (2.2σ). This means that for a *Planck* cosmological model, the TSZ signal that we measure is in tension with the predictions of most of these feedback models (except for the AGN 8.5 model). When using the Mead model in combination with the pressure profiles from hydrodynamical simulations, we obtained weaker constraints due to the extra nuisance parameters of the model, for which we did not assume any tight prior. In this case, the data could not discriminate between different baryonic prescriptions, but generally preferred halos less concentrated and more bloated compared to a NFW profile.

We then discussed whether the lack of tight priors on the nuisance parameters is limiting our analysis, finding that the Mead model parameters are dominating our prior volume. We discussed how one could place tighter constraints on the Mead model parameters measuring the matter profiles in hydrodynamical simulations for the range of halo masses to which our measurement is sensitive. Additional constraints on the Mead model parameters could also be provided by a joint analysis with cosmic shear, including small scales—possibly with a more coherent, physically motivated framework, as the one introduced in Mead *et al.* [59]. In general, it might also be useful to include in future analyses additional correlations sensitive to different halo masses (e.g., Compton-y galaxy cross-correlations or Compton-y autocorrelations) in order to be able to study feedback mechanisms over a wide range of halo masses. Last, we mentioned how future data and, in particular, future releases of the ACT Compton-y map (which will cover the full DES footprint) will improve our ability to discriminate between different feedback models, as these maps will allow us to measure with high accuracy the Compton-y shear correlation at small scales, where feedback models show a large variance. This will constitute a substantial improvement over current ACT data (which have a limited overlap with DES data and hence noisier cross-correlation measurements) and over *Planck* data, which have a low angular resolution that does not allow us to efficiently probe the small-scale regime.

The full Metacalibration catalog will be made publicly available following publication [82]. The code used to perform the tests in this manuscript will be made available upon request to the authors.

ACKNOWLEDGMENTS

This paper has gone through internal review by the DES and ACT Collaborations. S. P. is supported in part by the U.S. Department of Energy Award No. DE-SC0007901 and NASA ATP Grant No. NNH17ZDA001N. E. S. is supported by DOE Award No. DE-AC02-98CH10886. K. M. acknowledges support from the National Research Foundation of South Africa. Z. X. is supported by the Gordon and Betty Moore Foundation. J. P. H. acknowledges funding for SZ cluster studies from NSF AAG No. AST-1615657. Funding for the DES Projects has been provided by the U.S. Department of Energy, the U.S. National Science Foundation, the Ministry of Science and Education of Spain, the Science and Technology Facilities Council of the United Kingdom, the Higher Education Funding Council for England, the National Center for Supercomputing Applications at the University of Illinois at Urbana-Champaign, the Kavli Institute of Cosmological Physics at the University of Chicago, the Center for Cosmology and Astro-Particle Physics at The Ohio State University, the Mitchell Institute for Fundamental Physics and Astronomy at Texas A&M University, Financiadora de Estudos e Projetos, Fundação Carlos Chagas Filho de Amparo à Pesquisa do Estado do Rio de Janeiro, Conselho Nacional de Desenvolvimento Científico e Tecnológico, and the Ministério da Ciência, Tecnologia e Inovação, the Deutsche Forschungsgemeinschaft, and the collaborating institutions in the Dark Energy Survey. The collaborating institutions are Argonne National Laboratory, University of California at Santa Cruz, University of Cambridge, Centro de Investigaciones Energéticas, Medioambientales y Tecnológicas-Madrid, University of Chicago, University College London, DES-Brazil Consortium, University of Edinburgh, Eidgenössische Technische Hochschule (ETH) Zürich, Fermi National Accelerator Laboratory, University of Illinois at Urbana-Champaign, Institut de Ciències de l'Espai (IEEC/CSIC), Institut de Física d'Altes Energies, Lawrence Berkeley National Laboratory, Ludwig-Maximilians Universität München and the associated Excellence Cluster Universe, University of Michigan, National Optical Astronomy Observatory, University of Nottingham, The Ohio State University, University of Pennsylvania, University of Portsmouth, SLAC National Accelerator Laboratory, Stanford University, University of Sussex, Texas A&M University, and OzDES Membership Consortium. Based in part on observations at Cerro Tololo Inter-American Observatory at NSF's NOIRLab (NOIRLab Prop. ID 2012B-0001; PI: J. Frieman), which is managed by the Association of Universities for Research in Astronomy (AURA) under a cooperative agreement with the National Science Foundation. The DES data management system is supported by the National Science Foundation under Grants No. AST-1138766 and No. AST-1536171. The DES participants from Spanish institutions are partially supported by MINECO under Grants No. AYA2015-71825, No. ESP2015-66861, No. FPA2015-68048, No. SEV-2016-0588, No. SEV-2016-0597, and No. MDM-2015-0509, some of which include ERDF funds from the European Union. I. F. A. E. is partially funded by the CERCA program of the Generalitat de Catalunya. Research leading to these results has received funding from the European Research Council under the European Union's Seventh Framework Program

(FP7/2007-2013) including ERC Grant Agreements No. 240672, No. 291329, and No. 306478. We acknowledge support from the Brazilian Instituto Nacional de Ciência e Tecnologia (INCT) e-Universe (CNPq Grant No. 465376/2014-2). This manuscript has been coauthored by employees of Fermi Research Alliance, LLC under Contract No. DE-AC02-07CH11359 with the U.S. Department of Energy, Office of Science, Office of High Energy Physics. Support for ACT was through the U.S. National Science Foundation through Grants No. AST-0408698, No. AST-0965625, and No. AST-1440226 for the ACT project, as well as Grants No. PHY-0355328, No. PHY-0855887, and No. PHY-1214379. Funding was also provided by Princeton University, the University of Pennsylvania, and a Canada Foundation for Innovation (CFI) award to UBC. ACT operates in the Parque Astronomico Atacama in northern Chile under the auspices of the Agencia Nacional de Investigacion y Desarrollo (ANID). The development of multichroic detectors and lenses was supported by NASA Grants No. NNX13AE56G and No. NNX14AB58G. Detector research at N. I. S. T. was supported by the NIST Innovations in Measurement Science program.

APPENDIX A: VALIDATION ON N-BODY SIMULATIONS

We provide in this section further validation of our modeling by measuring the shear-Compton-y map cross-correlation on the fiducial DES Y3 N-body simulations. Note that an independent modeling check on hydrodynamical simulations has been performed by [42], validating the use of the halo framework to model shear-Compton-y cross-correlations.

For this test, we use one realization of the DES Y3 Buzzard catalog v2.0 [83,84]. Cosmological parameters of the simulation have been chosen to be $\Omega_{\rm m} = 0.286$, $\sigma_8 = 0.82$, $\Omega_b = 0.047$, $n_s = 0.96$, $h = 0.7$. The light cone of the simulation is generated on the fly starting from three boxes with different resolutions and sizes (1050^3, 2600^3, and 4000^3 Mpc^3 h^{-3} boxes and 1400^3, 2048^3, and 2048^3 particles); halos are identified using the public code ROCKSTAR [85] and they are populated with galaxies using ADDGALS [83]. Lensing effects are calculated using the multiple plane ray-tracing algorithm CALCLENS [86]. From the halo catalog, we construct a TSZ map by pasting a [43] profile on each halo. The map comes in the HEALPY format with a resolution of NSIDE 4096. For this test, we do not smooth the map nor add instrumental noise. As for the simulated shape catalog, we use for this test a shape noise-free catalog, which faithfully reproduces DES Y3 area coverage and number density. Galaxies are further divided into four tomographic bins following the same methodology used on data.

We measure $\xi^{\gamma_t y}$ using the unsmoothed, noise-free simulated Compton-y map over the *Planck* footprint and the shape noise-free simulated shear catalog. As Buzzard is a DM-only N-body simulation, we model the signal using a NFW profile for the Fourier transform of the DM profile, rather than the Mead model. The comparison between the theory predictions and our measurements in simulations is shown in Fig. 14. We only show the result of this comparison for scales larger than 20 arc min. Below such a scale, the simulation becomes unreliable, as the measurement points receive significant contributions from scales below the simulation resolution ($k = 3\ h/\mathrm{Mpc}$). In the scales where the comparison can be trusted, there is a very good match between the measurement and the theoretical predictions (the slight offset at large scales for bins 3 and 4 is compatible with cosmic variance, which is captured by the error bars). In particular, for the four tomographic bins, we obtain a $\chi^2 = 3, 4, 4, 5$ for 9 d.o.f.

As a final test, we fitted our measurements using the Mead model, rather than the NFW profile, fixing all the

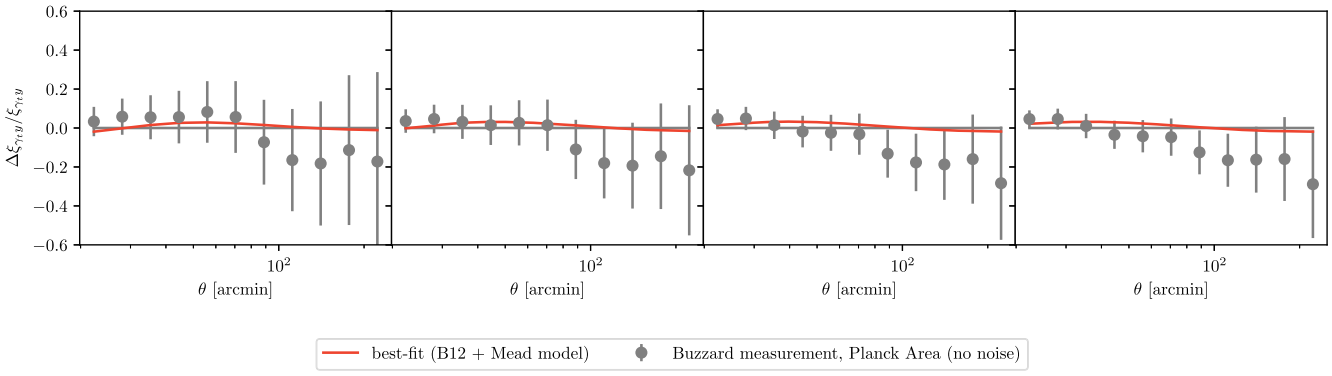

FIG. 14. Comparison between the measured $\xi^{\gamma_t y}$ in Buzzard simulation and our theory predictions. In particular, we report the fractional difference with respect to the theory predictions. Theory predictions have been obtained assuming a B12 pressure profile and NFW profile for the DM profile. Gray points represent the measurement on a unsmoothed, noise-free realization of Buzzard. Uncertainties are estimated using a noise-free theoretical covariance. Measurement points are very correlated (both among different redshift bins and angular scales). The red line represents the best fit to the data performed using the Mead model instead of the NFW profile.

parameters of our modeling except for the two Mead model parameters, which were sampled using broad flat priors. The Mead model encompasses the NFW profile as a subset of its parameter space, but it has additional flexibility. Indeed, the Mead model can provide a god fit for the Buzzard measurement at all scales.

APPENDIX B: COVARIANCE VALIDATION

We model the covariance $\mathbb{C}$ of the convergence and Compton-y cross-spectra as a sum of Gaussian ($\mathbb{C}^{\rm G}$) and non-Gaussian ($\mathbb{C}^{\rm NG}$) terms as follows:

$$\mathbb{C}(C_{\ell_1}^{\kappa,{\rm y_i}}, C_{\ell_2}^{\kappa,{\rm y_j}}) = \mathbb{C}^{\rm G}(C_{\ell_1}^{\kappa,{\rm y_i}}, C_{\ell_2}^{\kappa,{\rm y_j}}) + \mathbb{C}^{\rm NG}(C_{\ell_1}^{\kappa,{\rm y_i}}, C_{\ell_2}^{\kappa,{\rm y_j}}), \quad \text{(B1)}$$

where κ refers to the DES convergence field and y_i, y_j represent either the *Planck* or ACT Compton-y field. The Gaussian term is given by [87]

$$\mathbb{C}^{\rm G}(C_{\ell_1}^{\kappa,{\rm y_i}}, C_{\ell_2}^{\kappa,{\rm y_i}}) = \frac{\delta_{\ell_1\ell_2}}{f_{\rm sky}^{\kappa,{\rm y_i};\kappa,{\rm y_j}}(2\ell_1+1)\Delta\ell_1} \times [\hat{C}_{\ell_1}^{\kappa,\kappa}\hat{C}_{\ell_2}^{{\rm y_i},{\rm y_j}} + \hat{C}_{\ell_1}^{\kappa,{\rm y_j}}\hat{C}_{\ell_2}^{\kappa,{\rm y_i}}]. \quad \text{(B2)}$$

Here, $\delta_{\ell_1\ell_2}$ is the Kronecker delta, $f_{\rm sky}^{\kappa,{\rm y_i};\kappa,{\rm y_j}}$ is the effective sky coverage fraction, $\Delta\ell_1$ is the size of the multipole bin, and $\hat{C}_\ell$ is the total cross-spectrum between any pair of fields including the noise contribution. The non-Gaussian part, can be written following [88]

$$\mathbb{C}^{\rm NG}(C_{\ell_1}^{\kappa,{\rm y_i}}, C_{\ell_2}^{\kappa,{\rm y_j}}) = \frac{1}{4\pi f_{\rm sky}^{\kappa,{\rm y_i};\kappa,{\rm y_j}}} T_{\ell_1\ell_2}^{\kappa,{\rm y_i}\kappa,{\rm y_j}}, \quad \text{(B3)}$$

with

$$T_{\ell_1\ell_2}^{\kappa,y_i\kappa,y_j} = \int dz \frac{dV}{dz d\Omega} \int dM \frac{dn}{dM} \bar{\kappa}_{\ell_1}\bar{y}_{i,\ell_1}\bar{\kappa}_{\ell_2}\bar{y}_{j,\ell_2}. \quad \text{(B4)}$$

The real-space covariance for the measurement is then obtained by

$$\mathbb{C}(\xi^{\gamma_t y_i}(\theta_1), \xi^{\gamma_t y_j}(\theta_2)) = \int \frac{d\ell_1\ell_1}{2\pi} J_2(\ell_1\theta_1) \times \int \frac{d\ell_2\ell_2}{2\pi} J_2(\ell_2\theta_2)\mathbb{C}(C_{\ell_1}^{\kappa,{\rm y_i}}, C_{\ell_2}^{\kappa,{\rm y_j}}). \quad \text{(B5)}$$

In order to validate the covariance matrix, we follow [88] and perform a comparison with a covariance matrix estimated through jackknife resampling of the measurement on data. In particular, we use the following expression [74]:

$$\hat{\Sigma}(x_i, x_j) = \frac{(N_{\rm JK}-1)}{N_{\rm JK}} \sum_{k=1}^{N_{\rm JK}} (x_i^k - \overline{x_i})(x_j^k - \overline{x_j}), \quad \text{(B6)}$$

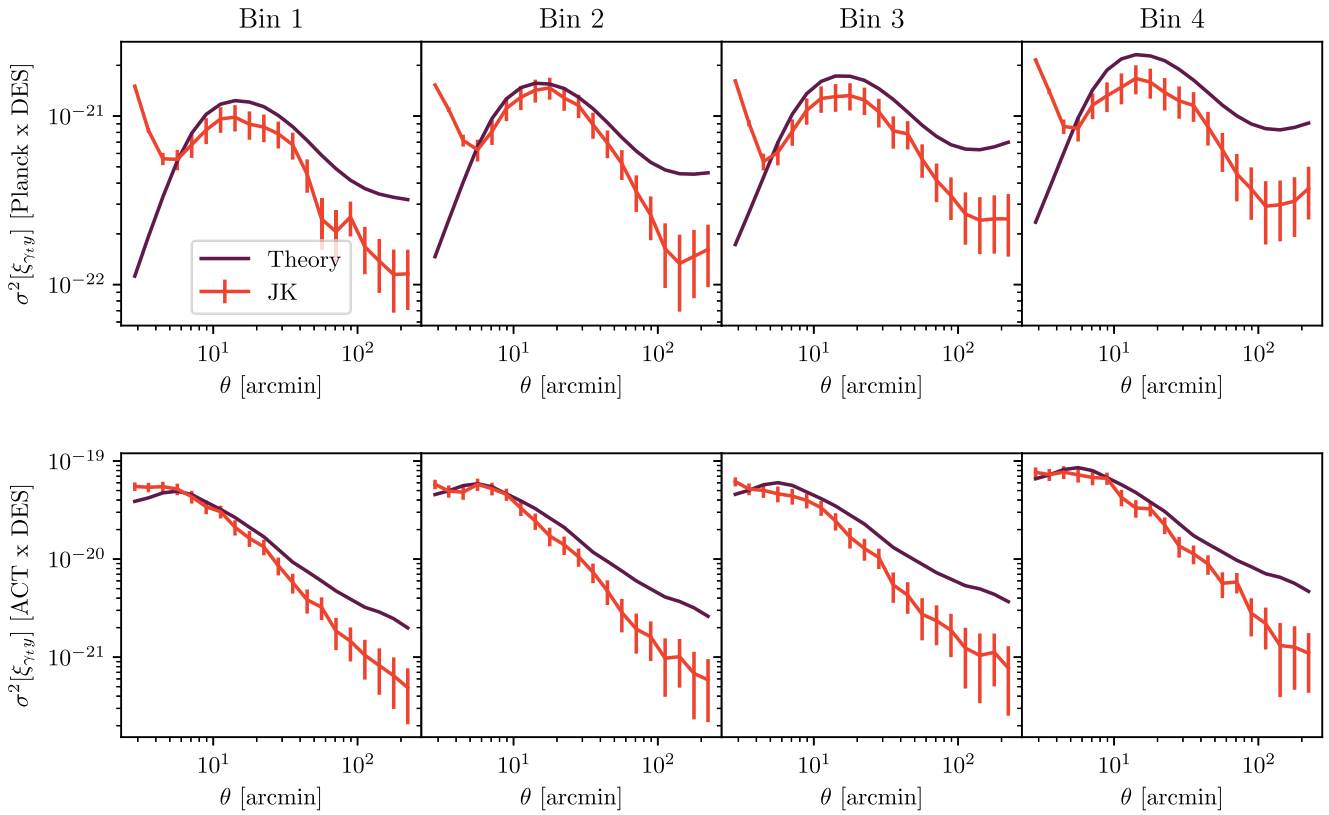

FIG. 15. Diagonal elements of the covariance matrix, for the *Planck* and DES $\xi^{\gamma_t y}(\theta)$ (top) and ACT and DES $\xi^{\gamma_t y}(\theta)$ (lower), for the four different DES tomographic bins. In each panel, we compare theory predictions (purple) to jackknife estimates (JK, red).

where the sample is divided into $N_{\rm JK} = 200$ subregions of roughly equal area, x_i is a measure of the statistic of interest in the ith bin of the kth sample, and $\overline{x_i}$ is the mean of our resamplings. Note that the jackknife resampling only allows one to efficiently estimate the covariance matrix on scales smaller than the size of the jackknife patches, so the jackknife covariance will be biased low at large scales. The comparison between the theoretical and the jackknife covariance for the $\xi^{\gamma_t y}$ measurements is shown in Fig. 15 and shows good agreement at small-intermediate scales, where the jackknife covariance can be considered reliable. Note that the range of scales where this comparison holds is smaller for ACT, since the average size of the JK patch is much smaller than in the case of *Planck*. In the case of *Planck* × DES covariance, the jackknife estimates have an upturn for scales smaller than 5 arc min which is not captured by our analytical covariance. Our guess is that this is related to mask effects; however, we did not investigate this further, as in the case of *Planck* × DES measurement we exclude scales <8 arc min due to *Planck* beam FWHM.

The $\xi^{\gamma_t y}$ measurement involving the DES and ACT map is also validated cross-correlating 300 simulated ACT maps with the DES Y3 shape catalog. These measurements should capture the dominant part of the Gaussian part of the covariance ($\propto \hat{C}^{\kappa,\kappa}_{\ell_1}\hat{C}^{y_i,y_j}_{\ell_2}$), but they cannot capture the terms $\hat{C}^{\kappa,y_j}_{\ell_1}\hat{C}^{\kappa,y_i}_{\ell_2}$ and the non-Gaussian part of the covariance, since the large-scale fluctuations of the simulated Compton-y maps are not correlated with the data one from the shear catalog. This is still a relevant comparison as these two latter terms should not dominate in the case of the ACT × DES measurement.

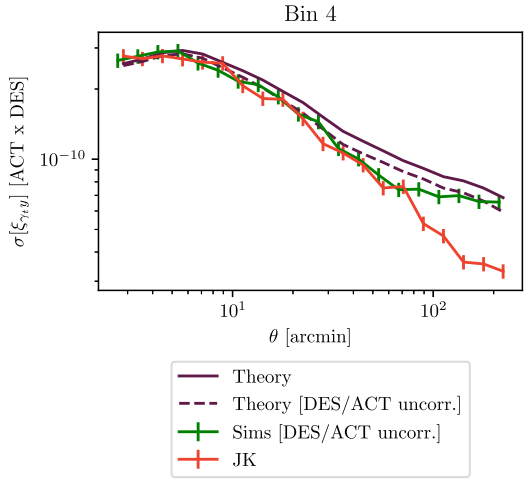

FIG. 16. Diagonal elements of the covariance matrix, for the fourth tomographic bin, for the ACT × DES $\xi^{\gamma_t y}(\theta)$. In addition to theory predictions (purple) and jackknife estimates (JK, red), we also show the estimates obtained by using ACT simulations and DES data (green) and the theory predictions that neglect correlations between ACT and DES (purple, dashed lines).

However, the non-Gaussian part of the covariance is expected to be subdominant when cross-correlating ACT with DES, so this should not strongly affect the comparison. Figure 16 shows the diagonal elements of the covariance matrix estimated using ACT simulations, showing a better match with theory at large scales compared to jackknife estimates. For comparison purposes, we also show the theory covariance matrix computed dropping terms that are not captured by the measurement in simulations.

APPENDIX C: TESTS ON WEBSKY MOCKS ON CIB CONTAMINATION

We further discuss in the Appendix the impact that the CIB can have on our measurements when the Compton-y maps are not generated by explicitly deprojecting the CIB signal. In our analysis, this has proven to be necessary for the *Planck* × DES measurement, whereas we found no significant CIB contamination of the ACT × DES signal, owing to the lower signal-to-noise ratio of the latter. To this aim, we use Websky mocks [89], which are full-sky simulations of the extragalactic microwave sky generated using the mass-peak patch approach. We use Compton-y, lensed CMB and CIB maps for frequencies 143, 217, 353, and 545 GHz, convolved with the nominal *Planck* Gaussian beam and with *Planck*-like white noise [32]. We created two sets of maps for each frequency channel: one with CIB contamination and one without CIB contamination. Last, we created three Compton-y maps using our NILC algorithm: a first map from the frequency channels without CIB contamination, a second map from the frequency channels with CIB contamination but without explicitly deprojecting the CIB signal, and a third one using the CIB contaminated frequency maps and deprojecting the CIB signal during the

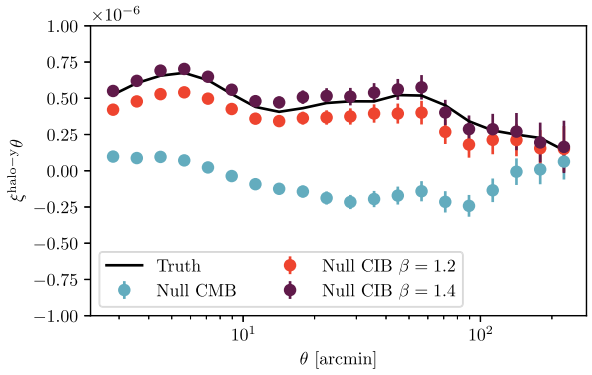

FIG. 17. Halo-Compton-y correlation from Websky mocks. The three different measurements use three different versions of the Compton-y maps. The black line refers to the case where the Compton-y map is created starting from frequency channels without CIB contamination, whereas the two other measurements have been obtained using frequency channels contaminated by a fiducial CIB signal, with or without CIB deprojection at the map-making level.

map-making process. When deprojecting the CIB signal, we used $\beta = 1.2$. The Websky mocks do not have shear maps available, but they provide a dark-matter halo catalog. To qualitatively span the same redshift and halo mass range probed by our measurement, we selected halos so as to have a sample with average mean redshift $\langle z \rangle \sim 0.25$ and average halo mass $10^{14.3}$ $M_\odot$. This corresponds to the typical redshift and halo mass of our measurement involving the fourth tomographic bin (see paper II). We then computed the halo Compton-y correlation signal (obtained cross-correlating the halos positions with the values of the Compton-y maps). We show in Fig. 17 the measurements with the three different Compton-y maps. The angular scale sensitivity of this halo-Compton-y correlation is expected to be different from the shear-Compton-y correlation; moreover, when creating the simulated Compton-y maps we did not use any frequency channels below 143 GHz, contrary to the maps on data. For these reasons, the effect of CIB on these measurements cannot be directly compared to the effect of CIB we see on data. Nonetheless, from Fig. 17 is clear that if no CIB deprojection is implemented when making the Compton-y map, the resulting measurement can be strongly biased.

APPENDIX D: TESTS OF FEEDBACK MODELS USING DES PRIOR

We show in this Appendix the constraints of feedback models obtained using DES priors on σ_8 and Ω_m. Table VI shows the best-fit χ^2 and the update-difference-in-mean tension for the different feedback scenarios, for both cases where we use the NFW rescaling to model the lensing part of our signal and where we use the Mead model instead. The posteriors of σ_8 and Ω_m are shown in Fig. 18. The main difference with respect to our analysis using the *Planck* prior (Sec. IV D) concerns the UDM tension metric, which does not show any sign of tension with the DES prior owing to the broader prior from the DES analysis compared to *Planck*. Besides this, similar to the *Planck* prior case, we find that when implementing the NFW rescaling, the data prefer the AGN 8.5 scenarios, whereas when implementing the Mead model, we are not able to discriminate among different feedback scenarios, owing to the less constraining nature of this modeling choice.

TABLE VI. Best fit χ^2 for the four feedback models (B12, AGN, AGN8.5, REF), obtained assuming *Planck* on σ_8 and Ω_m, and marginalizing over nuisance parameters as explained in Sec. III D. The top half of the table refers to the models obtained rescaling the NFW profile for the lensing signal; on the other hand, the bottom half of the table refers to the analysis where we model the lensing signal using the Mead model. We also report the UDM tension for the best-fit models with respect to their priors.

DES prior (NFW rescaling)					
	B12	AGN	AGN 8.5	REF	TNG
χ^2/d.o.f.	···	170/119	158/119	187/119	194/119
UDM tension	···	0.5σ	0.1σ	0.3σ	0.6σ

DES prior (free $A_{\rm Mead}$, $\eta_{\rm Mead}$)					
	B12	AGN	AGN 8.5	REF	TNG
χ^2/d.o.f.	154/118	154/118	154/118	156/118	154/118
UDM tension	0.7σ	0.2σ	0.3σ	0.2σ	053σ

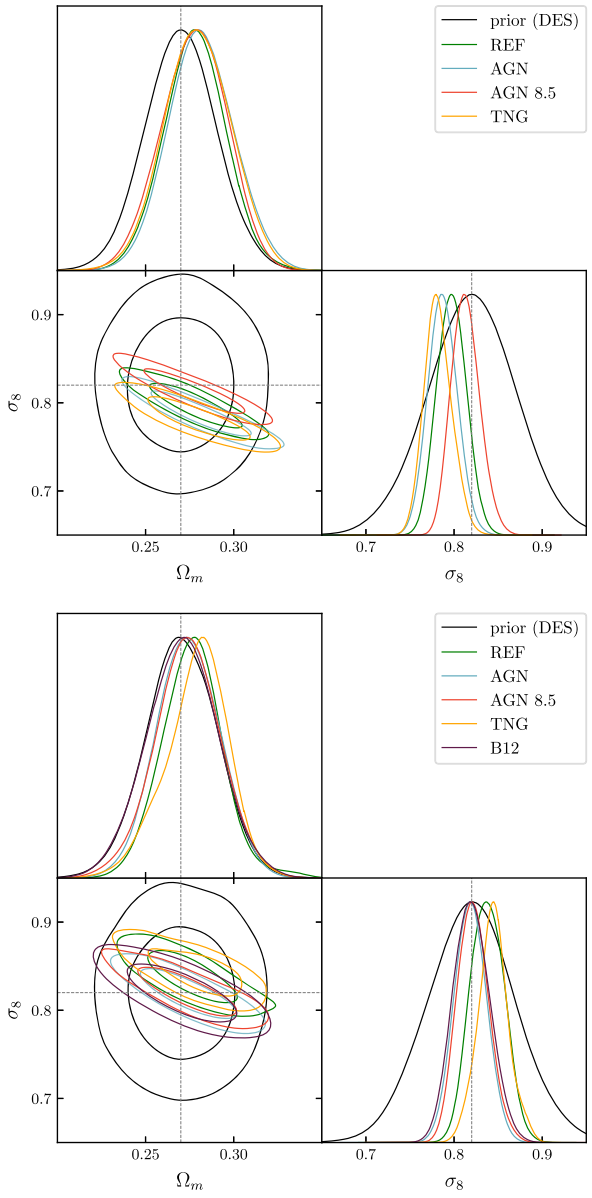

FIG. 18. Posterior for the parameters σ_8 and Ω_m for the four (five) feedback models: (B12), REF, AGN, AGN 8.5 and TNG. We also show the DES prior. Top refers to the case where we used the NFW rescaling to model the lensing part of our signal; the bottom plot refers to the more conservative analysis where we used the Mead model.

[1] R. A. Sunyaev and I. B. Zel'dovich, Annu. Rev. Astron. Astrophys. **18**, 537 (1980).
[2] R. A. Sunyaev and Y. B. Zel'dovich, Comments Astrophys. Space Phys. **4**, 173 (1972).
[3] E. Komatsu and U. Seljak, Mon. Not. R. Astron. Soc. **336**, 1256 (2002).
[4] B. Flaugher, H. T. Diehl, K. Honscheid *et al.*, Astron. J. **150**, 150 (2015).
[5] K. Kuijken, C. Heymans, H. Hildebrandt *et al.*, Mon. Not. R. Astron. Soc. **454**, 3500 (2015).
[6] H. Aihara, R. Armstrong, S. Bickerton *et al.*, Publ. Astron. Soc. Jpn. **70**, S8 (2018).
[7] P. A. Abell, J. Allison *et al.* (LSST Science Collaboration), arXiv:0912.0201.
[8] R. Laureijs, J. Amiaux, S. Arduini *et al.*, arXiv:1110.3193.
[9] N. E. Chisari, A. J. Mead, S. Joudaki *et al.*, Open J. Astrophys. **2**, 4 (2019).
[10] M. P. van Daalen, I. G. McCarthy, and J. Schaye, Mon. Not. R. Astron. Soc. **491**, 2424 (2020).
[11] M. P. van Daalen, J. Schaye, C. M. Booth, and C. Dalla Vecchia, Mon. Not. R. Astron. Soc. **415**, 3649 (2011).
[12] T. Eifler, E. Krause, S. Dodelson, A. R. Zentner, A. P. Hearin, and N. Y. Gnedin, Mon. Not. R. Astron. Soc. **454**, 2451 (2015).
[13] H.-J. Huang, T. Eifler, R. Mandelbaum, and S. Dodelson, Mon. Not. R. Astron. Soc. **488**, 1652 (2019).
[14] E. Semboloni and H. Hoekstra, and J. Schaye, Mon. Not. R. Astron. Soc. **434**, 148 (2013).
[15] M. A. Troxel, N. MacCrann, J. Zuntz *et al.*, Phys. Rev. D **98**, 043528 (2018).
[16] M. Asgari, C.-A. Lin, B. Joachimi *et al.*, Astron. Astrophys. **645**, A104 (2021).
[17] H. Hildebrandt, M. Viola, C. Heymans *et al.*, Mon. Not. R. Astron. Soc. **465**, 1454 (2017).
[18] S. Joudaki, C. Blake, C. Heymans *et al.*, Mon. Not. R. Astron. Soc. **465**, 2033 (2017).
[19] A. J. Mead, S. Brieden, T. Tröster, and C. Heymans, Mon. Not. R. Astron. Soc. **502**, 1401 (2021).
[20] A. J. Mead, C. Heymans, L. Lombriser, J. A. Peacock, O. I. Steele, and H. A. Winther, Mon. Not. R. Astron. Soc. **459**, 1468 (2016).
[21] C. Hikage, M. Oguri, T. Hamana *et al.*, Publ. Astron. Soc. Jpn. **71**, 43 (2019).
[22] H.-J. Huang, T. Eifler, R. Mandelbaum *et al.*, Mon. Not. R. Astron. Soc. **502**, 6010 (2021).
[23] L. Van Waerbeke, G. Hinshaw, and N. Murray, Phys. Rev. D **89**, 023508 (2014).
[24] J. C. Hill and D. N. Spergel, J. Cosmol. Astropart. Phys. 02 (2014) 030.
[25] A. Hojjati, T. Tröster, J. Harnois-Déraps *et al.*, Mon. Not. R. Astron. Soc. **471**, 1565 (2017).
[26] K. Osato, M. Shirasaki, H. Miyatake, D. Nagai, N. Yoshida, M. Oguri, and R. Takahashi, Mon. Not. R. Astron. Soc. **492**, 4780 (2020).
[27] M. Gatti, E. Sheldon, A. Amon *et al.*, Mon. Not. R. Astron. Soc. **504**, 4312 (2021).
[28] N. Aghanim, M. Arnaud *et al.* (Planck Collaboration), Astron. Astrophys. **594**, A22 (2016).
[29] M. S. Madhavacheril, J. C. Hill, S. Næss *et al.*, Phys. Rev. D **102**, 023534 (2020).
[30] S. Pandey *et al.* following paper, Phys. Rev. D **105**, 123526 (2022).
[31] P. A. R. Ade, N. Aghanim *et al.* (Planck Collaboration), Astron. Astrophys. **594**, A2 (2016).
[32] N. Aghanim, Y. Akrami *et al.* (Planck Collaboration), Astron. Astrophys. **641**, A3 (2020).
[33] J. Delabrouille and J. F. Cardoso, *Diffuse Source Separation in CMB Observations*, Lecture Notes in Physics Vol. 665 (Springer-Verlag, Berlin, Heidelberg, 2009), pp. 159–205.
[34] F. Guilloux, G. Fay, and J.-F. Cardoso, arXiv:0706.2598.
[35] S. Pandey, E. J. Baxter, Z. Xu *et al.*, Phys. Rev. D **100**, 063519 (2019).
[36] I. Sevilla-Noarbe, K. Bechtol, M. Carrasco Kind *et al.*, Astrophys. J. Suppl. Ser. **254**, 24 (2021).
[37] E. Huff and R. Mandelbaum, arXiv:1702.02600.
[38] E. S. Sheldon and E. M. Huff, Astrophys. J. **841**, 24 (2017).
[39] N. MacCrann, M. R. Becker, J. McCullough *et al.*, Mon. Not. R. Astron. Soc. **509**, 3371 (2021).
[40] J. Myles, A. Alarcon, A. Amon *et al.*, Mon. Not. R. Astron. Soc. **505**, 4249 (2021).
[41] A. Cooray and R. Sheth, Phys. Rep. **372**, 1 (2002).
[42] N. Battaglia, J. C. Hill, and N. Murray, Astrophys. J. **812**, 154 (2015).
[43] N. Battaglia, J. R. Bond, C. Pfrommer, and J. L. Sievers, Astrophys. J. **758**, 75 (2012).
[44] J. Tinker, A. V. Kravtsov, A. Klypin, Kevork Abazajian, Michael Warren, G. Yepes, S. Gottlöber, and D. E. Holz, Astrophys. J. **688**, 709 (2008).
[45] J. C. Hill and E. Pajer, Phys. Rev. D **88**, 063526 (2013).
[46] E. Komatsu and T. Kitayama, Astrophys. J. **526**, L1 (1999).
[47] J. L. Tinker, B. E. Robertson, A. V. Kravtsov, A. Klypin, M. S. Warren, G. Yepes, and S. Gottlöber, Astrophys. J. **724**, 878 (2010).
[48] A. M. C. Le Brun, I. G. McCarthy, and J.-B. Melin, Mon. Not. R. Astron. Soc. **451**, 3868 (2015).
[49] A. M. C. Le Brun, I. G. McCarthy, J. Schaye, and T. J. Ponman, Mon. Not. R. Astron. Soc. **441**, 1270 (2014).
[50] V. Springel, R. Pakmor, A. Pillepich, R. Weinberger, D. Nelson, L. Hernquist, M. Vogelsberger, S. Genel, P. Torrey, F. Marinacci, and J. Naiman, Mon. Not. R. Astron. Soc. **475**, 676 (2018).
[51] J. F. Navarro, C. S. Frenk, and S. D. M. White, Astrophys. J. **462**, 563 (1996).
[52] E. Moser, S. Amodeo, N. Battaglia, M. A. Alvarez, S. Ferraro, and E. Schaan, Astrophys. J. **919**, 2 (2021).
[53] W. A. Hellwing, M. Schaller, C. S. Frenk, T. Theuns, J. Schaye, R. G. Bower, and R. A. Crain, Mon. Not. R. Astron. Soc. **461**, L11 (2016).
[54] I. G. McCarthy, J. Schaye, S. Bird, and A. M. C. Le Brun, Mon. Not. R. Astron. Soc. **465**, 2936 (2017).
[55] J. Prat, J. Blazek, C. Sánchez *et al.*, arXiv:2105.13541.
[56] E. S. Sheldon, D. E. Johnston, J. A. Frieman, R. Scranton, T. A. McKay, A. J. Connolly, T. Budavári, I. Zehavi, N. A. Bahcall, J. Brinkmann, and M. Fukugita, Astron. J. **127**, 2544 (2004).
[57] A. J. Mead, J. A. Peacock, C. Heymans, S. Joudaki, and A. F. Heavens, Mon. Not. R. Astron. Soc. **454**, 1958 (2015).
[58] N. MacCrann, J. Aleksić, A. Amara *et al.*, Mon. Not. R. Astron. Soc. **465**, 2567 (2017).

[59] A. J. Mead, T. Tröster, C. Heymans, L. Van Waerbeke, and I. G. McCarthy, Astron. Astrophys. **641**, A130 (2020).
[60] S. Bridle and L. King, New J. Phys. **9**, 444 (2007).
[61] C. M. Hirata and U. Seljak, Phys. Rev. D **70**, 063526 (2004).
[62] E. Krause, T. F. Eifler, J. Zuntz *et al.*, arXiv:1706.09359.
[63] M. C. Fortuna, H. Hoekstra, B. Joachimi, H. Johnston, N. E. Chisari, C. Georgiou, and C. Mahony, Mon. Not. R. Astron. Soc. **501**, 2983 (2021).
[64] W. J. Handley, M. P. Hobson, and A. N. Lasenby, Mon. Not. R. Astron. Soc. **450**, L61 (2015).
[65] W. J. Handley, M. P. Hobson, and A. N. Lasenby, Mon. Not. R. Astron. Soc. **453**, 4385 (2015).
[66] N. Aghanim, Y. Akrami *et al.* (Planck Collaboration), Astron. Astrophys. **641**, A6 (2020).
[67] T. M. C. Abbott, F. B. Abdalla, A. Alarcon *et al.*, Phys. Rev. D **98**, 043526 (2018).
[68] S. Samuroff, J. Blazek, M. A. Troxel *et al.*, Mon. Not. R. Astron. Soc. **489**, 5453 (2019).
[69] M. Jarvis, G. Bernstein, and B. Jain, Mon. Not. R. Astron. Soc. **352**, 338 (2004).
[70] Y.-K. Chiang, R. Makiya, B. Ménard, and E. Komatsu, Astrophys. J. **902**, 56 (2020).
[71] S. J. Schmidt, B. Ménard, R. Scranton, C. B. Morrison, M. Rahman, and A. M. Hopkins, Mon. Not. R. Astron. Soc. **446**, 2696 (2015).
[72] M. Remazeilles, J. Delabrouille, and J.-F. Cardoso, Mon. Not. R. Astron. Soc. **418**, 467 (2011).
[73] P. A. R. Ade, N. Aghanim *et al.* (Planck Collaboration), Astron. Astrophys. **571**, A30 (2014).
[74] P. Norberg, C. M. Baugh, E. Gaztañaga, and D. J. Croton, Mon. Not. R. Astron. Soc. **396**, 19 (2009).
[75] M. H. Quenouille, Proc. Cambridge Philos. Soc. **45**, 483 (1949).
[76] Z. Yan, A. Hojjati, T. Tröster, G. Hinshaw, and L. Van Waerbeke, Astrophys. J. **884**, 139 (2019).
[77] E. Schaan, S. Ferraro, S. Amodeo *et al.*, Phys. Rev. D **103**, 063513 (2021).
[78] M. Shirasaki, Mon. Not. R. Astron. Soc. **483**, 342 (2019).
[79] P. A. R. Ade, N. Aghanim *et al.* (Planck Collaboration), Astron. Astrophys. **571**, A28 (2014).
[80] M. Raveri and W. Hu, Phys. Rev. D **99**, 043506 (2019).
[81] S. Naess, S. Aiola, J. E. Austermann *et al.*, J. Cosmol. Astropart. Phys. 12 (2020) 046.
[82] https://des.ncsa.illinois.edu/releases.
[83] J. DeRose, R. H. Wechsler, M. R. Becker *et al.*, arXiv:1901.02401.
[84] J. DeRose, R. H. Wechsler, M. R. Becker *et al.*, arXiv:2105.13547.
[85] P. S. Behroozi, R. H. Wechsler, and H.-Y. Wu, Astrophys. J. **762**, 109 (2013).
[86] M. R. Becker, Mon. Not. R. Astron. Soc. **435**, 115 (2013).
[87] W. Hu and B. Jain, Phys. Rev. D **70**, 043009 (2004).
[88] R. Makiya, S. Ando, and E. Komatsu, Mon. Not. R. Astron. Soc. **480**, 3928 (2018).
[89] G. Stein, M. A. Alvarez, and J. R. Bond, Mon. Not. R. Astron. Soc. **483**, 2236 (2019).